Centre Énergie Matériaux Télécommunications

EXPLORATION OF THE BAND STRUCTURE OF SOLIDS BY PHOTOEMISSION SPECTROSCOPY VIA BIAS VOLTAGE APPLIED TO THE SAMPLE AND WIDE ANGULAR ACCEPTANCE DEFLECTORS.

Par

Benson Kwaku Frimpong

Mémoire présenté pour l'obtention du grade de

Maître ès Sciences (M.Sc.)

en sciences de l'énergie et des matériaux

Jury d'évaluation

Président du jury et examinateur interne	Prof. Kenneth Beyerlein Institut National de la Recherche Scientifique
Examinateur externe	Prof. Giulio Vampa University of Ottawa
Examinateur interne	Prof. Kenneth Beyerlein Institut National de la Recherche Scientifique
Directeur de recherche	Prof. Fabio Boschini Institut National de la Recherche Scientifique

Dedication

I want to dedicate this work to all those who have been there for me this past year.

Acknowledgements

I would like to express my deepest gratitude to my supervisor, Professor Fabio Boschini, for his invaluable guidance, encouragement, and support throughout this research. My sincere thanks also go to my immediate supervisor, Dr. Nicolas Gauthier, for his close mentorship and continuous assistance during the course of this work.

I am grateful to all members of the Boschini Research Group, Dr. Francesco Goto, Akib Jabed, Dario Armanno, Jean-Michel Parent, and Shawn Lapointe, for their insightful discussions, technical support, and camaraderie.

I would also like to acknowledge the support received from the ALLS research team, particularly the technicians and research associates, whose assistance during beamtime experiments was essential.

A special note of thanks goes to Dr. Gaétan Jargot for his patient and thorough training on the laser systems, which was instrumental to the success of this project.

Abstract

Angle-Resolved Photoemission Spectroscopy (ARPES) is a fundamental tool in condensed matter physics for investigating the electronic structure of materials. By measuring the energy and momentum of electrons emitted from the surface of a material after photon excitation, ARPES maps directly their electronic band structures. These maps uncover vital details about phenomena such as superconductivity, excitonic behavior, charge density waves and spin-orbit coupling effects. Although high photon energy sources have traditionally been used in ARPES studies to access broad regions of momentum space, low photon energy sources have gained popularity because of their simpler experimental setups and cost efficiency, despite their more limited momentum range. Recent advances in ARPES instrumentation, including deflector technology, have enhanced the collection of photoemitted electrons, thereby broadening the in-plane momentum coverage. This innovation allows researchers to collect photoemitted electrons from a wider range of angles without needing to rotate the sample. In addition, the light matter interaction geometry is fixed, making it easier to model and understand the photoemission matrix elements. However, when using a hemispherical analyzer, current deflector designs are typically limited to a maximum acceptance range of around 60 degrees, leaving some electrons undetected. While momentum microscopes can detect all emitted electrons, the hemispherical analyzer remains crucial because it provides the highest energy and angular resolutions, which are essential for detailed electronic structure analysis. To overcome this limitation, applying an electric field between the sample and the analyzer can bend the electron trajectories, guiding more electrons into the analyzer’s aperture. This technique expands the accessible momentum range while maintaining consistent experimental conditions, preserving matrix elements and cross-sectional areas, and thus improving the reliability and quality of the data. This study builds on an existing approach that applies a bias voltage to a sample to enhance electron collection and convert emission angles into momentum space for a single direction in the plane, using a system without deflectors. The aim is to develop a more comprehensive method that incorporates deflectors and extends the angle-to-momentum conversion to both in-plane momentum directions, allowing for a complete characterization of the Fermi surface and a thorough assessment of the effectiveness of the expanded approach. The study uses Au(111) as a reference material to test the momentum conversion approach under various conditions. Additional materials, including WTe_2, $Bi_2Sr_2CaCu_2O_8$ (Bi2212), and Sr_2RuO_4, are employed to confirm that the model is not material dependent. In doing so, it seeks to uncover both the potential advantages, and the challenges associated with this technique in ARPES measurements to understand the electronic properties of materials.

Résumé

La spectroscopie de photoémission résolue en angle (ARPES) constitue un outil fondamental en physique de la matière condensée pour l'étude de la structure électronique des matériaux. En mesurant l'énergie et la quantité de mouvement des électrons émis depuis la surface d'un matériau à la suite d'une excitation lumineuse, l'ARPES permet de mesurer directement les structures de bandes électroniques. Ces structures de bandes révèlent des informations essentielles sur des phénomènes tels que la supraconductivité, les états excitoniques, les ondes de densité de charge ainsi que les effets du couplage spin-orbite.

Si les sources de photons à haute énergie ont longtemps été privilégiées dans les études ARPES en raison de leur capacité à sonder de larges régions de l'espace réciproque, les sources de photons à basse énergie suscitent un intérêt croissant, notamment pour leur mise en œuvre expérimentale simplifiée et leur coût réduit, malgré un accès plus limité de l'espace réciproque. Des avancées récentes, en particulier l'introduction de la technologie de déflecteurs, ont permis d'élargir la région mesurable de l'espace réciproque en améliorant la collecte des électrons photoémis. Cette technologie offre la possibilité de recueillir des électrons provenant d'un plus grand éventail d'angles d'émission, sans rotation de l'échantillon, tout en maintenant une géométrie d'interaction lumière-matière fixe, ce qui facilite l'interprétation du signal de photoémission.

Cependant, dans le cadre de l'utilisation d'un analyseur hémisphérique, les systèmes actuels de déflecteurs ne détectent que les électrons dans un cône d'émission d'environ 60 degrés, ce qui empêche la détection d'une partie des électrons émis. Bien que les microscopes de momentum permettent une détection complète, l'analyseur hémisphérique demeure incontournable en raison de sa résolution énergétique et angulaire supérieure, essentielle pour une analyse fine de la structure électronique.

Afin de dépasser cette limitation, l'application d'un champ électrique entre l'échantillon et l'analyseur peut courber les trajectoires électroniques, augmentant ainsi le nombre d'électrons collectés par l'analyseur. Cette approche élargit l'espace réciproque accessible tout en conservant des conditions expérimentales constantes, ce qui permet de préserver les éléments de matrice et les sections efficaces, améliorant ainsi la fiabilité et la qualité des données collectées.

Ce travail s'appuie sur une approche antérieure consistant à appliquer une tension électrique à l'échantillon pour améliorer la collecte des électrons et convertir les angles d'émission en quantité de mouvement dans une seule direction, en l'absence de déflecteurs. L'objectif est ici de développer une méthode plus globale, intégrant l'usage de déflecteurs et généralisant la conversion d'angle en momentum

aux deux directions dans le plan. Cette méthode vise à permettre une caractérisation complète de la surface de Fermi et à évaluer de manière rigoureuse l'efficacité de cette approche élargie.

Le matériau Au(111) est utilisé comme référence pour valider la conversion d'angle en momentum dans diverses conditions expérimentales. D'autres matériaux, tels que WTe_2, $Bi_2Sr_2CaCu_2O_8$ (Bi2212) et Sr_2RuO_4, sont également étudiés afin de démontrer l'indépendance du modèle vis-à-vis du matériau. Ce travail cherche ainsi à identifier les avantages potentiels ainsi que les défis inhérents à cette technique dans le cadre des mesures ARPES, en vue d'une meilleure compréhension des propriétés électroniques des matériaux.

Exploration de la structure de bande des solides par spectroscopie de photoémission, via l'application d'une tension électrique à l'échantillon et l'utilisation de déflecteurs.

Chapitre 1 : Introduction

La spectroscopie de photoémission résolue en angle (ARPES) est une technique puissante permettant d'étudier la structure électronique des matériaux en sondant l'énergie et le momentum des électrons émis après une excitation lumineuse. Les données obtenues par ARPES permettent de mesurer directement les bandes électroniques et de comprendre des phénomènes tels que la supraconductivité et les interactions des quasi-particules. Traditionnellement, des sources lumineuses avec des photons de haute énergie sont utilisées pour explorer une grande portion de l'espace réciproque, mais les sources de photons à basse énergie présentent également un intérêt important, car elles offrent une meilleure résolution et une mise en œuvre expérimentale simplifiée.

Les développements récents de l'instrumentation ARPES, comme l'introduction de déflecteurs électrostatiques, permettent d'élargir la région mesurable de l'espace réciproque sans avoir à faire pivoter l'échantillon, ce qui assure une grande stabilité expérimentale. Néanmoins, les déflecteurs actuels ont une une ouverture angulaire maximale d'environ soixante degrés, ce qui empêche la détection d'une partie des électrons photoémis. Pour pallier cette limitation, il est possible d'appliquer un champ électrique entre l'échantillon et l'analyseur afin de courber les trajectoires des électrons et de les guider vers le détecteur, augmentant ainsi l'espace réciproque accessible.

Ce travail s'appuie sur un modèle préexistant qui décrit comment l'application d'une tension électrique sur l'échantillon donnent accès à une région élargie de l'espace réciproque. Spécifiquement, ce travail étend le modèle à l'utilisation d'un analyseur hémisphérique avec déflecteurs. Cette approche permet de mesurer le momentum selon les deux axes du plan sans rotation de l'échantillon. En prenant un échantillon d'Au(111) comme référence, nous établissons une expression pour convertir les données de l'espace angulaire vers l'espace réciproque, en intégrant l'effet de la tension appliquée, et nous analysons l'influence de cette tension sur la résolution en énergie et momentum. Ce travail est séparé en cinq parties : la présentation de la théorie et de l'instrumentation ARPES, l'étude de l'application d'une tension életrique à l'échantillon et son modèle, la procédure expérimentale, l'analyse des résultats sur Au(111) et, finalement l'analyse sur d'autres matériaux.

L'ARPES repose sur un principe « photon entrant, électron sortant », où l'énergie et le momentum des électrons émis révèlent la structure électronique du matériau. Ce principe est fondé sur l'effet

photoélectrique, observé pour la première fois par Heinrich Hertz puis expliqué par Albert Einstein, qui reçut le prix Nobel en 1921 pour cette découverte. Lorsqu'une lumière monochromatique d'énergie hν frappe la surface d'un matériau et dépasse sa fonction de travail Φ, des photoélectrons sont émis. En résolvant leur énergie cinétique et leur angle d'émission, on accède aux informations électroniques fondamentales du solide. Les électrons sont émis dans toutes les directions, mais l'ARPES utilise un spectromètre de photoélectrons pour enregistrer leur énergie cinétique E_k et leurs angles d'émission θ et ϕ. L'angle θ correspond à l'angle polaire par rapport à la normale de surface, et ϕ à l'angle azimutal défini par la géométrie expérimentale. La relation de conservation de l'énergie s'écrit $E_b = h\nu - \Phi - E_k$, où E_b est l'énergie de liaison de l'électron. La conservation du momentum permet de relier les angles mesurés aux composantes dans le plan du momentum de l'électron dans le matériau. La composante hors plan, non strictement conservée, peut être déduite sous certaines hypothèses, tandis que le momenutm des photons est généralement négligeable pour les énergies de 6 à 100 eV.

Dans une expérience ARPES, les données enregistrées correspondent à l'intensité en fonction de l'énergie cinétique et des angles détectés. L'intensité mesurée est proportionnelle au carré de l'élément de matrice de photoémission et à la fonction spectrale de la particule, modulée par la fonction de Fermi-Dirac. Les informations sur la dispersion électronique peuvent être extraites sous forme de courbes de distribution en énergie (EDC) ou de courbes de distribution en momentum (MDC). Les EDC montrent l'intensité en fonction de l'énergie à momentum fixé, utiles pour étudier la structure fine et les pics de quasi-particules, mais parfois difficiles à interpréter pour la dispersion. Les MDC représentent l'intensité en fonction du momentum à énergie fixée et offrent généralement des profils plus symétriques, adaptés à un ajustement lorentzien permettant de déterminer avec précision les positions de pics et les taux de diffusion.

La source lumineuse utilisée en ARPES détermine l'énergie des photons et donc l'étendue de l'espace des moments accessible, ainsi que la profondeur sondée, qui correspond au libre parcours moyen inélastique des électrons. Les électrons détectés doivent quitter la surface sans subir de collisions inélastiques, ce qui rend l'ARPES intrinsèquement sensible à la surface. Les sources utilisées incluent les synchrotrons, les lampes à décharge gazeuse et les lasers. Dans ce travail, nous utilisons principalement une source laser de 6 eV, qui offre une excellente résolution en momentum et permet la détection de subtils détails dans la structure électronique malgré une couverture limitée de la zone de Brillouin.

L'analyseur hémisphérique constitue l'élément central de l'ARPES. Les électrons photoémis passent à travers une série de lentilles électrostatiques qui les focalise vers la fente d'entrée de l'analyseur. La largeur de cette fente détermine la gamme angulaire acceptée et influence directement la résolution énergétique et angulaire. À l'intérieur de l'analyseur, les électrons sont dispersés selon leur énergie cinétique en suivant des trajectoires courbes entre deux hémisphères, et atteignent un détecteur composé d'une galette de microcanaux (MCP), d'un écran de phosphore et d'une caméra numérique qui produit une image en énergie et en angle.

L'ajout de déflecteurs dans le systèmes de lentilles améliore considérablement la capacité de cartographier l'espace réciproque, en permettant de collecter les électrons provenant de différentes directions cristallographiques sans rotation de l'échantillon. Cette technologie assure une constance des éléments de matrice et des sections efficaces, ce qui est essentiel pour des mesures précises et rapides.

L'échantillon est monté sur une platine située dans une chambre à ultra-haut vide, avec une pression inférieure à 10^{-10} mbar. Cette platine permet de refroidir ou chauffer l'échantillon et assure le contact électrique nécessaire pour drainer le photocourant induit.

Ainsi, l'ARPES constitue une technique de choix pour explorer la structure électronique des matériaux à l'échelle quantique. Ce premier chapitre pose les bases théoriques et instrumentales nécessaires pour comprendre les chapitres suivants, qui détaillent l'effet de l'application d'une tension électrique sur l'échantillon, la méthodologie expérimentale et l'application de cette approche à divers matériaux.

Chapitre 2 : Application d'une tension électrique sur l'échantillon

L'application d'une tension électrique sur l'échantillon est une technique permettant de modifier l'énergie et la trajectoire des électrons émis depuis une surface. Dans la communauté ARPES, cette méthode a d'abord été employée pour corriger les différences de fonction de travail entre l'échantillon et l'analyseur.

Plus récemment, l'application d'un voltage négatif sur la surface de l'échantillon a ouvert une nouvelle voie dans l'exploration de l'espace réciproque. Lorsqu'une tension négative est appliquée, un champ électrique est généré et courbe les trajectoires des électrons photoémis, focalisant ainsi une gamme plus large d'angles d'émission vers l'entrée de l'analyseur. Cette approche permet d'accroître la couverture en momentum dans une seule configuration expérimentale, ce qui est particulièrement avantageux avec les photons de faible énergie, dont la portée en momentum est naturellement limitée.

L'application d'un voltage n'est cependant pas sans conséquences sur les données mesurées. Les électrons voient leur énergie cinétique modifiée par l'accélération post-émission et leurs angles d'émission se trouvent déformés au fur et à mesure qu'ils se déplacent du matériau vers l'analyseur. La relation entre l'angle à l'échantillon et l'angle détecté devient donc non linéaire, et un modèle de conversion des angles en momentum adapté est nécessaire pour interpréter correctement les spectres.

L'application d'une tension sur l'échantillon, combinée à un analyseur hémisphérique, permet d'élargir le région mesurée de l'espace réciproque en collectant les électrons issus d'une plus grande gamme d'angles d'émission. Il est important de noter que, sans voltage, un microscope de momentum pourrait détecter tous les électrons émis. Toutefois, l'analyseur hémisphérique reste crucial car il fournit la meilleure résolution angulaire et énergétique, indispensable à l'étude détaillée de la structure électronique. L'enjeu principal est de déterminer si l'augmentation de la région accessible de l'espace réciproque obtenue grâce au voltage se fait sans dégrader significativement la résolution.

Des études antérieures ont montré qu'aux faibles tensions appliquées, le spectre couvre une zone plus large du détecteur qu'à des tensions plus élevées. Ainsi, la meilleure résolution angulaire est obtenue pour les faibles tensions appliquées. À des tensions plus élevées, les électrons sont concentrés dans une zone plus restreinte du détecteur, ce qui tend à compresser les informations angulaires et à réduire la résolution dans cette dimension.

Sur l'axe de l'énergie, le voltage influence principalement l'énergie cinétique des électrons. L'accélération post-émission augmente l'énergie cinétique avant l'entrée dans l'analyseur, mais la fenêtre énergétique utile reste similaire lorsqu'elle est normalisée par rapport au niveau de Fermi. Les effets secondaires tels que la charge d'espace et la distorsion du champ électrique peuvent introduire un léger élargissement en énergie pour des grandes valeurs de voltage, mais dans des conditions contrôlées, l'impact reste limité.

Dans les travaux fondateurs, un modèle analytique sans paramètre libre a été proposé pour décrire ces effets et a été validé expérimentalement, mais il ne traitait que des électrons émis le long de la direction de la fente de l'analyseur. Notre travail étend ce modèle pour tenir compte des deux directions de momentum dans le plan, afin d'exploiter pleinement la technologie des déflecteurs.

Deux scénarios limites sont traditionnellement considérés pour la conversion des angles en moment. Le premier, appelé limite angulaire, suppose que l'angle détecté correspond exactement à l'angle à l'entrée de l'analyseur. Ce modèle, simple et proche de l'approche classique de l'ARPES, tend à surestimer le momentum pour de grande valeur de voltage. Le second, dit limite de position, se base sur la position des

électrons à l'entrée de l'analyseur et sur la courbure de leur trajectoire dans le champ électrique supposé uniforme entre l'échantillon et l'analyseur. Ce modèle tend à sous-estimer les valeurs de momentum. Ces deux limites sont utilisées comme bornes pour comparer les données expérimentales.

Afin de mieux décrire les mesures obtenues dans notre configuration, nous avons introduit une approche intermédiaire que nous appelons la limite de ratio. Elle représente un compromis entre la limite de position et la limite angulaire en combinant leurs contributions respectives à l'aide de coefficients pondérés dont la somme est égale à un. Cette flexibilité permet d'ajuster le modèle pour reproduire fidèlement la forme parabolique du seuil d'émission à basse énergie (LEC, Low Energy Cutoff) observée expérimentalement. La limite de ratio s'adapte ainsi à différents matériaux et conditions expérimentales, tout en conservant un sens physique clair en termes de trajectoire électronique.

Le modèle a été étendu pour corriger également l'intensité mesurée dans l'espace réciproque. La conversion d'une représentation angulaire à une représentation en momentum nécessite une transformation jacobienne qui prend en compte le changement de coordonnées en deux dimensions. Cette correction d'intensité est essentielle pour obtenir des surfaces de Fermi quantitatives, où l'intensité mesurée reflète fidèlement la densité d'états.

En conclusion, ce chapitre établit le cadre théorique de l'effet de l'application d'une tensition électrique sur un échantillon dans les expériences ARPES et présente le modèle étendu permettant de convertir les angles détectés en momentums tout en corrigeant l'intensité. Cette approche jette les bases pour mesurer des surfaces de Fermi bidimensionnelles et de l'étude approfondie de la structure électronique dans des conditions expérimentales non conventionnelles utilisant à la fois une tension appliquée et des déflecteurs.

Chapitre 3 : Matériaux et procédure expérimentale

Ce chapitre décrit en détail les instruments, les matériaux et les procédures expérimentales utilisés dans cette étude. L'ensemble des expériences a été réalisé à la station tr-ARPES du laboratoire ALLS à Varennes, au Québec, qui est équipée d'un système ARPES à analyseur hémisphérique SPECS ASTRAIOS intégrant la technologie des déflecteurs. Cette configuration permet une large couverture angulaire et offre trois modes de détection : Medium Angle Mode (MAM) avec une acceptation de 20°, Wide Angle Mode (WAM) avec 40°, et Super Wide-Angle Mode (SWAM) avec 60°. Ces modes permettent d'optimiser la collecte des électrons photoémis selon les conditions expérimentales et la résolution recherchée.

La source lumineuse utilisée dans cette étude est un faisceau laser de 6 eV issu d'un laser Yb:YAG de 1030 nm et 50 W. Les photons de 6 eV sont obtenus à l'aide de cristaux non linéaires. Le processus commence par la génération de 515 nm (deuxième harmonique), suivie d'une somme de fréquences pour produire 343 nm, puis 206 nm (correspondant à 6 eV). La taille du faisceau sur l'échantillon est d'environ 70 µm. Cette source de photons à basse énergie offre une excellente résolution en momentum et est adaptée à la détection de détails subtils dans la structure électronique.

L'ensemble des mesures a été réalisé dans des conditions d'ultra-haut vide, avec une pression de base inférieure à 10^{-10} mbar dans les chambres d'analyse et de préparation. La chambre de préparation est équipée d'une source d'ions pour la pulvérisation cathodique et d'un chauffage par faisceau d'électrons permettant le recuit des échantillons. La chambre d'analyse est équipée d'un analyseur hémisphérique avec un système de lentilles électrostatiques, de déflecteurs et d'un détecteur 2D. Le système est conçu pour collecter les électrons dans une large plage angulaire tout en préservant la résolution énergétique.

L'application de voltage sur l'échantillon a été réalisée à l'aide d'une alimentation DC Hewlett Packard 6228B. La tension est appliquée à l'échantillon par l'intermédiaire du connecteur de chauffage par faisceau d'électrons, qui assure également la mise à la masse. Cette configuration permet d'appliquer des tensions négatives comprises entre quelques volts et plusieurs dizaines de volts, afin de courber les trajectoires des électrons photoémis et d'élargir la couverture en momentum.

Le matériau principal étudié est l'or, Au(111), choisi pour sa surface bien définie et son état de surface clair. Sa structure électronique est bien connue, ce qui en fait un matériau de référence pour valider les méthodes de conversion des angle en momentum et les performances instrumentales. La préparation de l'Au(111) a consisté en des cycles de pulvérisation cathodique et de recuit. L'échantillon a été bombardé par des ions Ar+ pendant environ 30 minutes, puis recuit progressivement jusqu'à 900 K avant d'être refroidi lentement à température ambiante. Ces cycles ont permis de nettoyer la surface et de restaurer la périodicité atomique nécessaire à une bonne photoémission de surface.

D'autres matériaux ont été étudiés afin de tester la généralité de la méthodologie. Le premier est WTe_2, un matériau fortement anisotrope dont la structure électronique varie selon la direction cristallographique. L'étude de ses spectres ARPES avec l'application d'un tension électrique permet de comparer les dispersions obtenues pour différentes orientations de la fente de l'analyseur et de déterminer la direction offrant la meilleure résolution. La préparation de WTe_2 a nécessité un clivage in

situ à basse température sous ultra-vide, après collage d'une petite tige en céramique avec une colle d'argent.

Le second matériau est $Bi_2Sr_2CaCu_2O_8+\delta$ (Bi2212), un supraconducteur à haute température critique. Sa surface de Fermi est dominée par les plans CuO_2 et présente un pseudo-gap et des effets de repliement de bandes dus à des modulations structurales. L'application d'un voltage pendant la mesure ARPES permet d'accéder simultanément aux régions nodales et antinodales de la surface de Fermi, ce qui est crucial pour l'étude des dynamiques électroniques en tr-ARPES. L'échantillon a été préparé de la même manière que WTe_2, par clivage in situ à basse température et sous ultra-vide.

Le troisième matériau est Sr_2RuO_4, un supraconducteur non conventionnel à structure pérovskite en couche. Sa surface de Fermi présente une symétrie tétragonale et des effets de « nesting » caractéristiques. L'accès à ces caractéristiques est difficile avec des photons de 6 eV en raison de l'accès limité en momentum. L'application d'un voltage permet de collecter des électrons sur une plus large portion de la zone de Brillouin et de caractériser des distorsions éventuelles de la symétrie ou des effets de « nesting ».

Des mesures spécifiques ont été réalisées pour chaque matériau. Pour Au(111), une dépendance de la tension électrique a été effectué allant de −5 V à −30 V, afin d'observer comment la région de momentum accessible et la résolution sont affectées. Des tests de dépendance de la largeur de fente, de 0,1 mm à 1 mm, ont permis d'évaluer l'impact sur la résolution angulaire et la netteté des surfaces de Fermi. Des mesures de dépendance du flux lumineux ont été menées pour identifier d'éventuels effets de charge d'espace et d'élargissement en énergie.

Pour WTe_2, des mesures de dépendance de la tension de −15 V à −35 V ont été réalisées à température ambiante pour comparer la région de momentum accessible selon la tension appliquée. Pour Bi2212 et Sr_2RuO_4, les mesures ont été effectuées respectivement à −35 V et −90 V, afin d'accéder à la plus grande portion possible de l'espace réciproque avec notre source de 6 eV.

Ce chapitre établit ainsi la base méthodologique et instrumentale de l'étude. Il présente le système ARPES utilisé, les matériaux sélectionnés et leur préparation, ainsi que les paramètres expérimentaux choisis . L'ensemble de ces informations est essentiel pour comprendre et interpréter les résultats détaillés présentés dans les chapitres suivants.

Chapitre 4 : Analyse sur Au(111)

Ce chapitre présente une analyse détaillée des mesures ARPES effectuées sur l'or Au(111), qui sert de matériau de référence pour valider la méthodologie développée dans ce travail. Les expériences sur Au(111) permettent de tester la robustesse du modèle de conversion des angles en momentum sous différentes conditions expérimentales et de caractériser l'influence de la tension électrique sur la résolution énergétique et en momentum.

La première partie de l'analyse concerne la comparaison des trois modes de détection de l'analyseur hémisphérique SPECS ASTRAIOS, à savoir le Super Wide-Angle Mode (SWAM), le Wide-Angle Mode (WAM) et le Medium Angle Mode (MAM). Les spectres mesurés dans les deux directions par rapport à la fente, parallèle et perpendiculaire, sont analysés afin de déterminer le mode offrant le meilleur compromis entre couverture en angle, facilité d'alignement et qualité des données. Les résultats montrent que le SWAM, bien que couvrant la plus large plage angulaire, est très sensible aux désalignements, ce qui complique l'acquisition de données fiables. Le MAM, à l'inverse, permet une bonne définition mais tronque une partie du spectre, car tous les électrons ne sont pas collectés. Le WAM se révèle être le mode optimal : il offre une large couverture, un alignement stable et un compromis satisfaisant entre les limites angulaire et de position, ce qui le rend idéal pour les mesures dépendantes du voltage.

L'étape suivante consiste à valider la conversion des angles en momentum à l'aide du modèle proposé dans le chapitre 2, basé sur la limite de ratio. Les courbes de seuil d'émission à basse énergie (Low Energy Cutoff, LEC) sont ajustées dans les deux directions de momentum, kx et ky, et superposées aux spectres expérimentaux. Les ajustements paraboliques montrent une excellente cohérence entre le modèle et les données, confirmant la pertinence de la limite de ratio pour décrire la conversion des angles en momentum dans notre configuration instrumentale incluant des déflecteurs et une tension électrique.

Une analyse de la surface de Fermi d'Au(111) a été réalisée pour différentes tensions appliquées. Elle montre qu'une tension plus élevée permet de collecter des électrons émis à de plus grands angles, élargissant la couverture en momentum. Les états de surface observés, formant des cercles, présentent un diamètre de 0,38 $Å^{-1}$, en bon accord avec les valeurs de la littérature, ce qui valide la précision de la conversion. L'étude de l'influence du voltage sur la résolution énergétique montre que l'élargissement en énergie reste minimal, inférieur à 2 meV, et relativement constant pour toutes les tensions testées. Ainsi, l'application d'un voltage n'altère pas de manière significative l'axe énergétique, ce qui est essentiel pour préserver la qualité spectrale dans les expériences ARPES.

L'impact de la largeur de la fente de l'analyseur a également été étudié. Les mesures effectuées à −30 V pour des fentes allant de 0,1 mm à 1 mm montrent que la réduction de la largeur de fente améliore la résolution en momentum, en particulier dans la direction perpendiculaire à la fente, tout en réduisant l'intensité collectée. Les surfaces de Fermi deviennent plus nettes à mesure que la fente se rétrécit, et les deux états de surfaces d'Au(111) sont mieux définis. Cette observation confirme que le choix de la fente représente un compromis entre résolution et flux d'électrons détectés.

Des mesures de dépendance au flux lumineux ont été menées pour examiner les effets de charge d'espace et d'élargissement énergétique. Les résultats montrent qu'à mesure que le flux augmente, la largeur à mi-hauteur (FWHM) des pics énergétiques et des distributions en momentum s'élargit légèrement. Cet élargissement résulte de la répulsion coulombienne entre électrons émis quasi simultanément. Les résultats obtenus à flux élevé révèlent également une légère courbure du niveau de Fermi, ainsi qu'une perte de netteté en fonction du momentum, indiquant que la charge d'espace devient significative à fort taux de comptage.

Ce chapitre démontre que l'application d'une tension électrique combinée à l'usage des déflecteurs permet d'élargir considérablement la couverture en espace des moments pour des photons de faible énergie, tout en préservant la haute résolution propre à l'analyseur hémisphérique. La limite de ratio développée se révèle robuste pour décrire la conversion des angles en momentum dans les deux directions, et l'ensemble des résultats obtenus sur Au(111) valide la méthodologie expérimentale et théorique proposée. Ces conclusions servent de base solide pour l'application de la technique à d'autres matériaux plus complexes, présentée dans le chapitre suivant.

Chapitre 5 : Résultats sur d'autres matériaux

Après avoir validé la méthodologie expérimentale et le modèle de conversion des angles en momentum sur l'or Au(111), nous avons étendu notre étude à d'autres matériaux afin d'évaluer la généralité et la robustesse de l'approche développée. Les matériaux choisis sont WTe_2, Sr_2RuO_4 et $Bi_2Sr_2CaCu_2O_8+\delta$ (Bi2212). Chacun d'entre eux présente des propriétés électroniques particulières qui permettent de tester la méthode dans des conditions variées et sur des surfaces de Fermi aux géométries distinctes.

Le premier matériau étudié est WTe_2, un semi-métal à forte anisotropie dont la structure électronique varie significativement selon la direction cristallographique. Les mesures ARPES ont été réalisées avec des tensions électrique comprises entre −15 V et −35 V. Les résultats montrent que l'application d'un voltage permet d'élargir la couverture en momentum et de révéler clairement les états électroniques

caractéristiques de WTe_2. Les directions Γ-X et Γ-M ont été comparées afin d'évaluer l'influence de l'anisotropie sur la résolution et la netteté des spectres. Il a été observé que la direction Γ-X fournit des dispersions plus nettes et des pics plus resserrés, tandis que la direction Γ-M présente des bandes plus diffuses. À mesure que la tension appliquée augmente, la couverture en momentum s'étend, mais une limitation instrumentale apparaît pour de larges tensions, où certaines trajectoires d'électrons atteignent les bords du détecteur.

Le second matériau étudié est Sr_2RuO_4, un supraconducteur non conventionnel à structure pérovskite en couche, dont la surface de Fermi présente une symétrie tétragonale et des effets de « nesting » prononcés. Les mesures ont été réalisées à une tension élevée de −90 V, afin d'explorer une large portion de la zone de Brillouin malgré la faible énergie de la source lumineuse (6 eV). Les surfaces de Fermi obtenues mettent en évidence les caractéristiques attendues, notamment la symétrie tétragonale et les sections parallèles de la surface de Fermi responsables du « nesting ». L'application d'un voltage élevé a permis d'accéder à des régions habituellement inaccessibles avec des photons de basse énergie, démontrant l'efficacité de la tension pour élargir la couverture en momentum. Les résultats montrent également que la limite de ratio appliquée dans les deux directions de momentum fournit une conversion cohérente et adaptée à ce matériau complexe.

Le troisième matériau, Bi2212, est un supraconducteur à haute température critique dont la surface de Fermi est dominée par les plans CuO_2 et présente des caractéristiques nodales et antinodales cruciales pour l'étude des propriétés supraconductrices et du pseudo-gap. L'un des défis de l'ARPES à basse énergie est d'obtenir en une seule mesure la cartographie complète de la surface de Fermi de Bi2212, en particulier pour accéder simultanément aux régions nodales et antinodales. L'application d'un voltage négatif a permis d'élargir considérablement la portion de l'espace des moments accessible et de capturer, dans une seule prise, les principaux arcs de la surface de Fermi. Cette capacité est particulièrement importante pour les expériences de tr-ARPES, où l'acquisition rapide et efficace est cruciale pour suivre l'évolution temporelle de la structure électronique après une excitation optique.

Dans les trois matériaux, la méthodologie développée s'est révélée robuste et indépendante de la nature du matériau. La conversion des angles en momentum par limite de ratio a fourni des résultats cohérents et physiquement interprétables, et l'application d'une tension électrique combinée à l'usage de déflecteurs a permis d'élargir la couverture de l'espace réciproque sans perte significative de résolution énergétique. Cette approche permet de dépasser les limitations traditionnelles de l'ARPES ayant une

source de photons à basse énergie et de réaliser des mesures plus complètes de la surface de Fermi dans une seule configuration expérimentale.

En conclusion, ce chapitre confirme que la stratégie expérimentale développée, validée sur Au(111), est applicable à des matériaux plus complexes et anisotropes. Les résultats obtenus sur WTe_2, Sr_2RuO_4 et Bi2212 démontrent la pertinence et la flexibilité de la méthodologie proposée, ouvrant la voie à une exploration plus complète et plus efficace de la structure électronique des matériaux quantiques avec des techniques ARPES combinant tension électrique et déflecteurs.

Chapitre 6 : Conclusion

Ce travail a porté sur l'exploration de la structure de bandes des solides par spectroscopie de photoémission résolue en angle (ARPES), en combinant l'application d'une tension électrique sur l'échantillon et l'utilisation de déflecteurs. L'objectif principal était d'élargir la couverture de l'espace réciproque tout en conservant une excellente résolution énergétique et angulaire, afin de mieux caractériser les surfaces de Fermi et les propriétés électroniques de matériaux quantiques.

Les expériences menées ont démontré que l'application d'une tension négative sur l'échantillon permet de courber les trajectoires des électrons photoémis, de focaliser un plus grand nombre d'électrons vers l'analyseur hémisphérique et ainsi d'accroître la portion accessible de l'espace réciproque. Combinée à la technologie des déflecteurs, cette approche a permis de réaliser une cartographie bidimensionnelle complète sans avoir à faire pivoter l'échantillon, ce qui réduit les temps d'acquisition et améliore la stabilité expérimentale.

Le modèle de conversion des angles en moment développé dans ce travail, basé sur la limite de ratio, s'est révélé particulièrement robuste. En introduisant une position intermédiaire entre la limite angulaire et la limite de position, ce modèle a permis d'obtenir une description fidèle des trajectoires électroniques et des paraboles du seuil d'émission à basse énergie. Son extension bidimensionnelle, couplée à une correction d'intensité par transformation jacobienne, a permis de produire des mesures quantitatives de l'espace réciproque, indispensables pour l'interprétation des surfaces de Fermi.

La méthodologie a été validée d'abord sur Au(111), matériau de référence aux états de surface bien connus. Les mesures ont montré que la tension électrique élargit la couverture en momentum sans altérer de façon significative la résolution énergétique, qui est restée inférieure à 2 meV. L'étude de la dépendance de la largeur de fente et au flux lumineux a permis de comprendre l'impact de ces paramètres sur la

résolution et sur les effets de charge d'espace. Les résultats obtenus sont en excellent accord avec la littérature et confirment la fiabilité de l'approche.

La méthode a ensuite été appliquée à des matériaux plus complexes : WTe_2, Sr_2RuO_4 et Bi2212. Dans tous les cas, la stratégie expérimentale combinant voltage et déflecteurs s'est révélée efficace et indépendante de la nature du matériau. Elle a permis d'accéder à des portions élargies de la zone de Brillouin, de révéler des caractéristiques anisotropes et de cartographier simultanément des régions nodales et antinodales, ce qui est particulièrement pertinent pour des études futures en tr-ARPES.

En conclusion, ce mémoire propose une avancée significative dans l'optimisation des mesures ARPES utilisant des sources de photons à basse énergie. Elle démontre que l'application d'une tension électrique sur l'échantillon, combinée à un analyseur hémisphérique équipé de déflecteurs, permet une exploration plus complète et plus rapide de l'espace récripoque, tout en maintenant des résolutions énergétiques et angulaires élevées. Cette approche offre un fort potentiel pour l'étude des matériaux émergents, en particulier dans des expériences dépendantes du temps, où la rapidité et la précision des mesures sont essentielles.

Les perspectives ouvertes par ce travail incluent l'application de cette méthodologie à des systèmes encore plus complexes, tels que les supraconducteurs non conventionnels, les matériaux topologiques et les hétérostructures à deux dimensions, ainsi que son intégration dans des expériences de tr-ARPES à haute cadence pour explorer les dynamiques électroniques ultrarapides avec une couverture complète de l'espace réciproque.

Table of Contents

List of figures

List of Abbreviation

ARPES	Angle Resolved Photoemission Spectroscopy
EDC	Energy Distribution Curve
MDC	Momentum Distribution Curve
LEC	Low Energy Cutoff
ALLS	Advanced Laser Light Source
RL	Ratio Limit
ELAA	Angular Limit
ELAP	Position Limit
TR-ARPES	Time-resolved ARPES
SWAM	Super Wide-Angle Mode
MAM	Medium Angle Mode
WAM	Wide Angle Mode

Chapter one: Introduction

Angle-Resolved Photoemission Spectroscopy (ARPES) is a powerful technique for studying the electronic structure of materials by probing the energy and momentum of electrons emitted after photon excitation [1], [2]. The data acquired in ARPES enable researchers to map the electronic band structure and understand phenomena like superconductivity and quasiparticle interactions[3], [4] . Typically, high-photon-energy light sources[5], [6], [7] are used for broader momentum exploration, but low-photon-energy sources are also valuable for their ease to setup and high-resolution [8], [9].

Recent advancements in ARPES instrumentation, such as deflector technology allow comprehensive in-plane momentum mapping without rotating the sample, preserving experimental consistency. However, current deflectors have a limited acceptance angle of 60 degrees, restricting the detection of some photoemitted electrons. To overcome this, an electric field can be applied between the sample and analyzer to focus all emitted electrons into the detector, enhancing the momentum range accessible in ARPES experiments.

This work builds on an existing model for expanding the momentum field view by applying sample bias [10] by using a hemispherical analyzer with deflectors to map the in-plane momentum without the need to rotate the sample. Using Au(111) as the main case study, we derive an expression to convert the data from angle to momentum incorporating the applied bias voltage and characterize how the bias voltage affects the energy and momentum resolution. The document is organized into five parts: introduction of ARPES theory and instrumentation, Sample biasing and its theory, experimental setup, studies on Au(111) and studies on other materials.

Angle-Resolved Photoemission Spectroscopy process and geometry.

ARPES is a photon-in electron-out technique for probing the energy and momentum of electrons to reveal the electron structure of materials [1], [2]. The basic principle of ARPES is the photoelectric effect which was first observed by Henry Hertz[11] and later explained by Albert Einstein[12] for which he won the Noble prize in 1921. That is, when a monochromatic light with energy hv hits a surface of a material and it is able to overcome the work function (Φ) of the material, photoelectrons are ejected from the surface [13]. By resolving the energy and emission angle of the photoelectrons, one can gain information about the properties of the material from which the photoelectrons came from and hence ARPES has been one of the leading techniques in revealing fundamental electronic properties of solid-state materials.

In the photoemission process, photoelectrons are emitted in all possible directions. However, to analyze them, a photoelectron spectrometer is used to record the kinetic energy of the photoemitted electrons (E_k) and their emission angles (θ, φ) .The θ emission angle refers to the polar angle with respect to the surface normal to the sample while the φ emission angle refers to the azimuthal angle which is defined with respect to the experimental geometry or crystal axis as shown in fig. 1.1 [13].

The binding energy (E_B) can be determined by relating the energy of the emitted electron (E_k) to the energy of the absorbed photon (hv) , while accounting for the material's work function (ϕ). This relationship is governed by energy conservation, where the binding energy is the difference between the photon energy and the sum of the work function and the kinetic energy of the electron:

$$E_B = hv - \phi - E_k \tag{1}$$

Momentum conservation also provides the remaining relationship between the measured electrons emission angles and the in-plane momentum ($k_{||}$), which is conserved due to translational symmetry before they were ejected from the sample. The out-of-plane component of momentum which is not conserved in the photoemission process can still be deduced using certain assumptions. Also, the momentum component of the incoming photon is typically ignored for photon energies 6eV-100eV because their momenta is negligible compared to the lattice momentum of most solids measured with ARPES. $k_{||}$ can be further divided into two orthogonal components k_x and k_y, which corresponds to the momentum in the directions defined by θ and the φ emission angles:

$$\overrightarrow{k_{||}} = \overrightarrow{k_x} + \overrightarrow{k_y} \tag{2}$$

$$k_{||} = \frac{1}{\hbar}\sqrt{2mE_k}sin\theta \tag{3}$$

$$k_x = \frac{1}{\hbar}\sqrt{2mE_k}sin\theta cos\varphi \tag{4}$$

$$k_y = \frac{1}{\hbar}\sqrt{2mE_k}sin\theta sin\varphi \tag{5}$$

Where $k_{||}$, k_x, and k_y are the modulus of the vectors $\overrightarrow{k_{||}}$, $\overrightarrow{k_x}$ and $\overrightarrow{k_y}$ respectively.

In an ARPES measurement, the data given is a map of intensity as a function of detected angles and kinetic energy. The measured intensity can be written as:

$$I(k,\omega) = I_0(k, v, \boldsymbol{A})A(k,\omega)f(\omega) \tag{6}$$

Where k is the electron momentum, ω is the electron energy with respect to the Fermi energy, $f(\omega)$ is the Fermi-Dirac function. $I_0(k, v, \boldsymbol{A})$ is proportional to the squared photoemission matrix element (where $\boldsymbol{A}$ is the electromagnetic vector potential) and $A(k,\omega)$ is the single-particle spectral function which contains information about electron dispersion and lifetime. There are two main methods to derive dispersion from an ARPES intensity map: energy distribution curve (EDC) analysis and momentum distribution curve (MDC) analysis. EDCs represent intensity as a function of energy at fixed momentum, providing insights into the spectral function, line shape, and details of the electronic structure, such as the presence of sharp quasiparticle peaks and energy gaps due to superconducting or charge density wave transitions. However, EDCs can be challenging to use for precise band dispersion due to factors like Fermi-Dirac distribution effects and background contributions. MDCs, on the other hand, display intensity as a function of momentum at fixed energy, typically yielding a more symmetric line shape that can be easily fitted with a Lorentzian function. This allows for accurate determination of peak positions, scattering rates, and dispersion by analyzing the peak position across different energies.

The basic ARPES setup consists of three main components to obtain a photoemission signal from the sample. This includes the light source/photon energy, the photoelectron analyzer and lastly the sample stage.

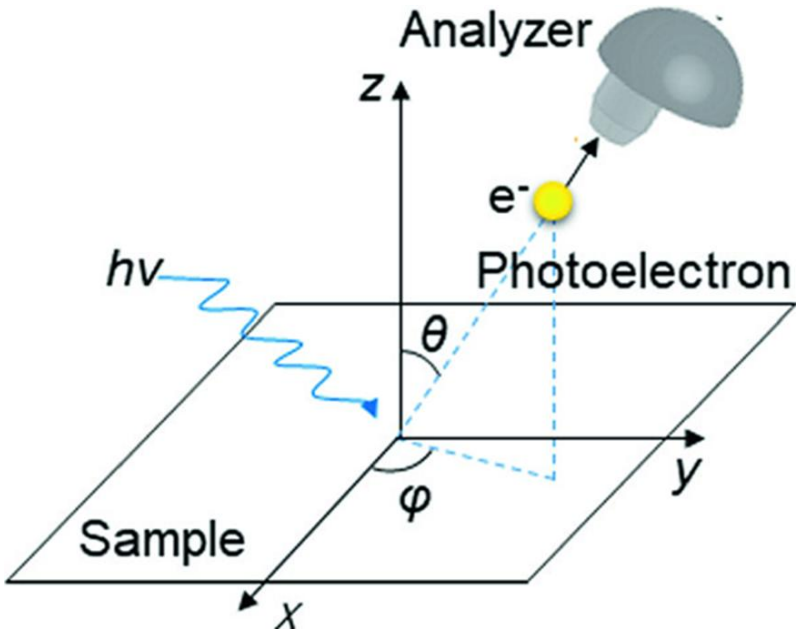

Figure 1. 1: The photoemission geometry. This diagram illustrates the basic geometry of an ARPES experiment, where incident photons (hv) strike the sample and excite electrons (photoelectrons) from the material. The emitted photoelectron is characterized by its emission angle θ (relative to the surface normal) and azimuthal angle φ[14]

Light source

In ARPES, the light source determines the photon energy of the probe, and it determines the accessible electronic dispersion for both E_B and $k_{||}$ (from eqn 1 and eqn 3). The photon energy also determines the probing depth of ARPES measurements. For a photoelectron to contribute to the detectable ARPES signal, it must travel through the material and escape from the surface without undergoing inelastic collisions. Consequently, the probing depth of ARPES is determined by the inelastic mean free path of electrons in solids, which is typically much shorter than the light's penetration depth and follows an energy dependence described by the universal mean free path for electrons in solids [15]. Depending on the photon energy, the probing depth can vary from a few to several Angstroms. This allows ARPES measurements to be surface or bulk sensitive. The light source's bandwidth (monochromaticity or energy resolution) and brightness directly affect the energy resolution of the collected ARPES data, and the efficiency of data acquisition needed to obtain sufficient statistical quality in ARPES measurements respectively. ARPES intensity is mostly strongly dependent on both the photon energy and photon polarization which is due to the dipole matrix element that modulate the photoemission process. There are three main light sources for ARPES measurement namely synchrotron light sources[5], [6], [7], [16],

gas discharge lamps[17] and the laser sources[8], [9], [18], [19]. Each of these light sources has its unique characteristics but the purpose of this work we will concentrate on laser-based sources.

Laser-based light sources are regarded as low photon energy sources and hence have a smaller momentum reach compared to their counterparts. Equation (3) sets the limit for the accessible $k_{||}$. Considering an ARPES setup where all photoelectrons can be collected at an emission angle of 90°, and using a photon energy of 6 eV, the maximum $k_{||}$ we can access is ±0.75 Å^{-1} for a material with a work function of 4.5 eV, as shown in Figure 1.2 [20]. This value is slightly smaller than the Brillouin zone size (1.6 Å^{-1}) of most studied materials with a lattice constant of 4 Å. Despite this disadvantage it has gained popularity mainly due to its easy setup and cost[21]. Also, due to its reduced momentum range, it allows for precise mapping of electronic states with minimal broadening leading to better momentum resolution which is beneficial for probing subtle features of electronic structures. One of the most significant advancements in ARPES with low photon energies is its integration with time-resolved ARPES (TR-ARPES). The high momentum resolution achieved at low photon energies allows for the detection of even small changes in the band structure as they evolve over time, which is particularly important for capturing dynamic processes in TR-ARPES. Despite all the advantages of low photon energies, there are certain limitations, with the most notable being the restricted momentum range, which limits the extent of the Brillouin zone that can be accessed.

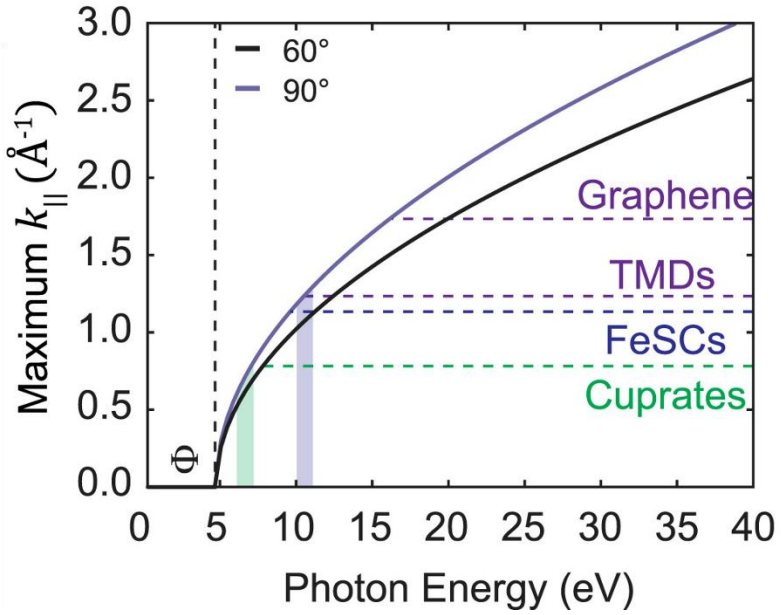

Figure 1. 2: The maximum accessible parallel momenta $k_{||}$ as a function of photon energy for emission angles 60°, and 90°. Horizontal dashed lines indicate the BZ boundary of several classes of materials. The available photon energies from 6-eV sources

and THG in gases are indicated by shaded regions green and blue, respectively. The work function is Φ = 4.5 eV. TMD: Transition-metal dichalcogenides. FeSCs: Iron-based superconductors [20] .

Photoelectron Analyzer

The photoelectron analyzer is central to ARPES experiments, as it is used to acquire the kinetic energy and emission angles of photoemitted electrons. Basic ARPES data span a three-dimensional phase space ($E_k - k_x - k_y$), which corresponds to the full range of electron momenta and energies that can be detected. Since photoemitted electrons can only escape into vacuum, their emission directions are restricted to a 2π steradians hemisphere. Various photoelectron analyzers can be used to analyze this data, but in this work, we focus on the hemispherical analyzer. This basically consists of a long cylindrical electrostatic lens column, a hemispherical energy analyzer, and an electron detector.

Electrostatic lens column

The lens column is typically located between the sample and the entrance of the hemispherical analyzer because it focuses electrons from the sample emission to the analyzer. In this description, we focus on the ASTRAIOS lens column by SPECS as shown in figure 1.3, as other systems may differ slightly[22].

The column begins with the objective lens, which allows for wide acceptance angles (up to ±30°) and minimizes spherical aberration to collect electrons from the sample. This lens focuses the electrons into a sharp real-space image, preserving angular and momentum information. The wide angular acceptance ensures efficient collection and allows for detailed electronic structure mapping.

Next in the column is the single spot parallel shifting lens, referred to as the octupole deflector. This deflector is critical for maintaining electron trajectory by converting the divergent electron beam into a parallel bundle. The shifting electrode in this plane enables full momentum-space mapping without rotating the sample. By adjusting the electric field, the momentum image is shifted, allowing access to different regions of k-space. This is essential to the ASTRAIOS system, as it facilitates comprehensive electron detection from a range of angles.

Following the deflector, the electrons encounter the motorized virtual entrance slit, a unique feature of the ASTRAIOS design. Rather than being located at the hemispherical analyzer's entrance, the slit is positioned in an electron-optical equivalent plane (RP1) within the lens column. This configuration allows electrons to pass through at much higher kinetic energies, which enhances resolution and detector homogeneity. The slit can be adjusted to control both angular and energy resolution, allowing for flexibility in various experimental conditions.

After passing through the slit, the electrons are guided by the second lens stage, which projects the electron image toward the entrance of the hemispherical analyzer. This lens preserves the angular and energy information of the electrons, ensuring that the analyzer receives an undistorted, high-resolution dataset.

The pass energy (E_p) is the kinetic energy of electrons as they enter the hemispherical analyzer, crucial for controlling the energy resolution. Before reaching the analyzer, electrons are accelerated or decelerated in the lens column, governed by the retarding ratio (R_r). The retarding ratio is defined as the ratio of the initial kinetic energy of the electrons (before entering the retarding field) to the pass energy.

A higher retarding ratio improves energy resolution because the analyzer can precisely separate electrons of slightly different kinetic energies. This is because the analyzer operates effectively when electrons move slower (i.e., lower pass energy), allowing for better dispersion of the electron energy spectrum. The relationship between energy resolution (ΔE) and the retarding ratio is inversely proportional, meaning that as the retarding ratio increases, the system's ability to resolve fine energy differences improves. However, there is a trade-off: a higher retarding ratio means fewer electrons are transmitted efficiently through the system, leading to a reduction in the electron count rate.

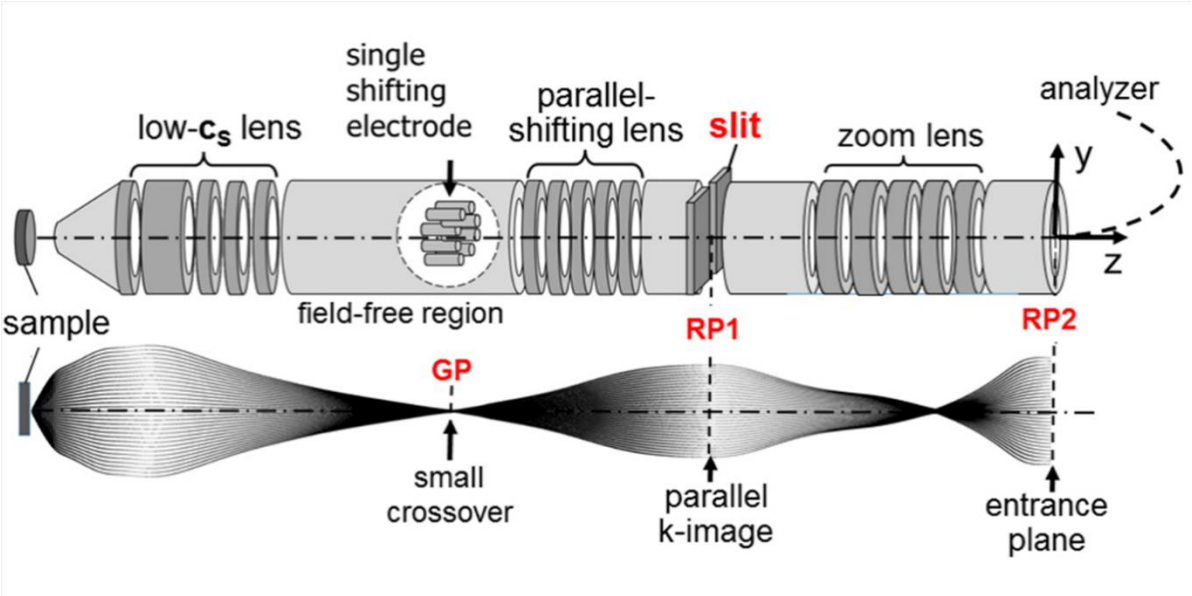

Figure 1. 3: Schematic of the ASTRAIOS lens column guiding electrons from the sample to the hemispherical analyzer. Starting with the low-Cs lens, which collects and focuses electrons from the sample, the electrons pass through the single shifting electrode (octupole deflector) to convert the divergent beam into a parallel bundle. The electrons then travel through the parallel-shifting lens and are directed via the virtual entrance slit located at the RP1 plane for energy and angular adjustments. The zoom lens further focuses the beam towards the RP2 entrance plane, preparing the electrons for energy analysis in the hemispherical analyzer [22].

Analyzer entrance slit.

In a hemispherical analyzer, the width of the entrance slit (d) is a critical factor that determines which photoemitted electrons can enter the analyzer for energy and momentum analysis. The slit, typically positioned at the entrance of the hemisphere analyzer, acts as a physical aperture, selectively allowing electrons to pass through based on their emission angle. The slit width, along with the pass energy and the radius of the hemispherical analyzer, significantly affects the energy resolution. A narrower slit restricts the range of electron angles that can pass through, limiting the range of electron trajectories. This tighter angular acceptance reduces the spread of electrons reaching the detector, focusing more specifically on those that follow near-ideal paths.

By narrowing the range of angles, the analyzer is more selective, ensuring that only electrons with trajectories that closely match the optimal energy reach the detector. This results in improved energy resolution, as the system can more precisely differentiate between closely spaced energy levels. The relation is given as below.

$$\Delta E = E_p \left(\frac{d}{2R} + \frac{\alpha^2}{2} \right) \tag{7}$$

Where α represents the angular acceptance of the slit and R the radius of the hemispherical analyzer.

Hemispherical energy Analyzer

The hemispherical analyzer is a commonly used type of analyzer in ARPES experiments. It operates by dispersing photoemitted electrons along a curved path between two concentric hemispherical electrodes with radii R_1 (inner radius) and R_2 (outer radius), as shown in Figure 1.4. The potential difference applied across these electrodes creates an electric field that forces the electrons to follow curved trajectories, thereby separating them based on their kinetic energy. Electrons with lower kinetic energy follow tighter trajectories within the hemisphere, while those with higher kinetic energy follow wider orbits. Electrons with kinetic energy matching the analyzer's pass energy will follow the ideal path and reach the detector, while others will deviate from this path.

Electrons passing through the analyzer are recorded by an electron detector, typically consisting of a multichannel plate (MCP) electron multiplier, a phosphor screen, and a digital camera. This detector records a 2D photoelectron image at the exit of the hemisphere, corresponding to a slice through the 3D phase space with one axis representing the kinetic energy and the other representing the emission angle

in the direction of the slit. The complete electronic structure in the 3D phase space can be obtained by sequentially scanning the other angular dimension, either by rotating the sample relative to the spectrometer or by using electrostatic deflectors that operate perpendicularly to the analyzer slit.

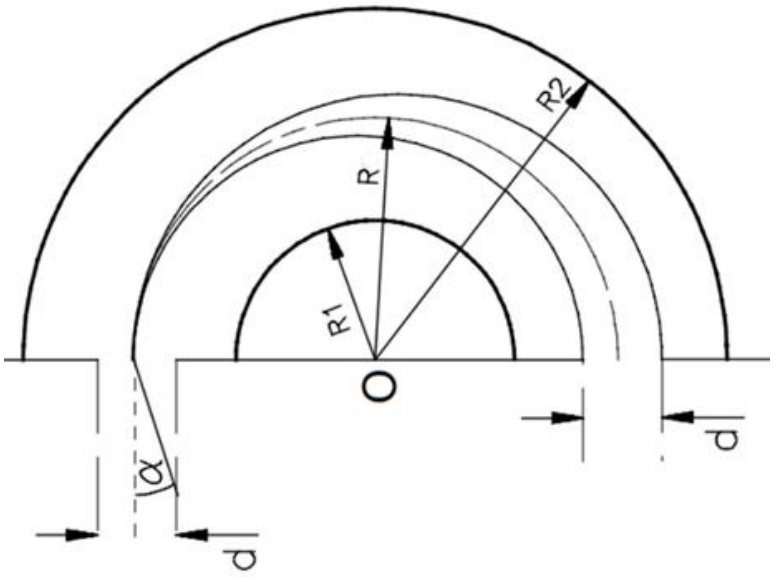

Figure 1. 4: Hemispherical Analyzer with two hemispheres of radius R1 and R2, slit width d for entrance and exit. R corresponds to the trajectory the electron takes to reach the detector[23]

Deflectors

Deflectors, such as those found in the electrostatic lens column of the ASTRAIOS system, are not typically present in conventional electrostatic lens columns of standard ARPES systems. Introducing deflectors into the lens column transforms a conventional hemispherical analyzer into something similar to a momentum microscope[23], [24], [25]. This modification allows for full mapping of the 3D phase space without needing to physically rotate the sample. The deflectors, in the form of an octupole, achieve this capability by applying an electric field that steers the trajectories of photoemitted electrons, enabling the simultaneous collection of electrons from both in-plane crystallographic directions. This approach maintains consistent cross-sectional areas and matrix elements, ensuring experimental accuracy. One of the key advantages of using deflectors is that they reduce the need for mechanical adjustments during experiments. This not only speeds up data acquisition but also minimizes mechanical vibrations and other artifacts, thereby improving the quality of the measurements.

Sample stage.

This is the stage where samples are mounted for photoemission measurements and since ARPES is a surface sensitive experiment, it is always key that this environment is an Ultra-High Vacuum chamber with a base pressure better than 10^{-10} mbar [26]. This stage is providing certain degrees of freedom for aligning and scanning different momentum space or direction within the sample. In ARPES, since the sample must be conductive in order to drain the total induced photocurrent, it is very important to have a good electrical contact with the sample and a ground which is provided by the sample stage which is also usually grounded to the ARPES system itself [24]. This contact also helps control the temperature of the sample, that's either to cool down to cryogenic temperatures or heating up to higher temperatures.

Chapter Two: Sample Biasing

Sample biasing is a technique to manipulate the behavior of electrons or other charged particles emitted from a sample. The technique involves applying an external voltage to the sample, which can alter the energy, trajectory, or emission characteristics of particles such as electrons, emitted from the sample.

In the ARPES community, sample biasing has been utilized for various purposes, including correcting work function differences between the sample and the analyzer[13].

In recent years, the application of a bias voltage in ARPES has taken on a new direction. By applying a negative voltage to the surface of the sample, an electric field is generated that bends the trajectories of the photoemitted electrons, effectively focusing a broader range of emission angles into the entrance of the analyzer[10], [27], [28]. This method increases the accessible momentum range in a single experimental setup, which is particularly important when using low-energy photons that naturally limit the momentum range. However, applying a bias voltage also alters the kinetic energy and emission angles of the electrons as they travel from the sample surface to the analyzer. The relationship between the emission angle at the sample and the angle measured by the detector becomes more complex, requiring a modified angle-to-momentum conversion model.

Though sample biasing, when coupled with a hemispherical analyzer, broadens the momentum field view by allowing the collection of photoemitted electrons from a wider range of angles, it is important to note that without applying sample bias, the momentum microscope analyzer can still detect all emitted electrons. However, the hemispherical analyzer remains crucial for providing the highest energy and angular resolution, both of which are necessary for detailed electronic structure analysis. This raises an important question: does the enhanced momentum coverage offered by the hemispherical analyzer come at the expense of resolution?

From references [10] and [27], it is evident that at lower applied bias voltages, the spectrum covers a larger portion of the detector compared to higher bias voltage values. At low voltage, the angular spread is the widest, allowing the spectrum to cover a larger portion of the detector. As the bias voltage increases, the angular spread narrows, resulting in reduced detector coverage. This trend suggests an inverse

relationship between the applied bias voltage and the extent of angular coverage on the detector. Consequently, we assume that the resolution is directly influenced by this change in coverage.

At lower bias voltages, the photoelectrons are distributed across a wider angular range, which allows the detector to resolve finer angular features, improving angular resolution. With more angular information available, the detector can more accurately distinguish small variations in emission angles. However, at higher bias voltages, the angular spread is much narrower, concentrating the electrons into a smaller area on the detector. While the angular features are still present, they are broadened due to being concentrated into a smaller region. This compression of angular information leads to a decrease in angular resolution, as the finer angular details become less distinguishable due to their concentration in a smaller area range on the detector.

In terms of how bias affects the energy axis, as the bias voltage increases, the electrons' kinetic energy increases due to post-emission acceleration. To maintain comparable energy windows across different bias voltages, the retarding ratio—the ratio of kinetic energy to pass energy—can be adjusted accordingly. Despite the increase in kinetic energy, the energy spread(window) remains constant and the bias should not have a significant effect on the energy broadening.

Reference [10] provided an analytical, parameter-free model to account for these changes, which has been validated by their experimental results. However, their model and experiments primarily accounts for photoemitted electrons along the slit orientation. In the subsequent section, we will introduce this model briefly and propose an expansion to cover both in-plane momentum directions.

Existing Model

The energy conservation equation (Equation 1) was modified to calculate both the kinetic energy detected (E_D) and the kinetic energy at the surface of the sample (E_s). This modification incorporates the bias voltage (U_B) and the work functions of both the sample (Φ_s) and the analyzer (Φ_A). For simplicity, a term called effective bias voltage (U_B^*) was introduced to account for the difference in work functions between the sample and the analyzer.

$$E_B = h\nu - \Phi_s - E_s \tag{8}$$

$$E_s = E_D + eU_B^* \tag{9}$$

$$U_B^* = U_B + (\Phi_A - \Phi_s)/e \tag{10}$$

Two scenarios were proposed for the angle-to-momentum conversion. In the first scenario, termed the angular limit, the assumption is that the angle at which the electron enters the analyzer (θ_{A}) will be the same angle detected on the detector (θ_{D}). This model follows the conventional angle-to-momentum conversion used in standard ARPES systems, where momentum is computed using the detector's angle directly. However, experimental results showed that this model overestimates the detected momentum at higher bias voltages, leading to inaccurate interpretations. In the second scenario, called the position limit, the primary factor is the position of the electrons as they enter the analyzer. This scenario requires to evaluate how the electric field between the sample and the analyzer bends the trajectories of the photoelectrons, as illustrated in Figure 2.1b. The model considers electron kinematics and acceleration by the electric field to derive an electron trajectory with bias voltage, assuming a uniform electric field, similar to that of a parallel plate capacitor. The derived conversion for both limits is given as:

$$k_{||} = \frac{1}{\hbar}\sqrt{2mE_s}Fsin\theta_{\mathrm{D}} \tag{11}$$

Where F is a scaling factor which accounts for bias voltage.

For the angular limit:

$$F = \sqrt{1 + 2\alpha} \tag{12}$$

For the position limit:

$$F = \sqrt{\frac{\alpha + 1 + \sqrt{2\alpha + 1 - \alpha^2 tan^2\theta_{\mathrm{D}}}}{2}} \tag{13}$$

$$\alpha = \frac{-eU_B^*}{2E_s} \tag{14}$$

In their work, the photoemission threshold known as the Low Energy Cutoff (LEC) is used to benchmark the angle-to-momentum conversion. The LEC is defined as the energy threshold below which photoemission cannot occur, because electrons lack the sufficient energy to overcome the material's surface potential barrier. Electrons with energy just above the LEC have enough energy to escape the surface and reach the detector, while those with energy below the LEC are unable to escape and are instead trapped by the surface potential. The LEC follows a parabolic shape, which arises from the relationship between the electron's kinetic energy and momentum. This behavior is influenced by both the material's work function and the energy of the incident photon.

$$E_{LM} = \frac{\hbar^2 k_{||}^2}{2m} \tag{15}$$

$$E_{LAP} = -eU_B^* \left[1 + (\frac{\tan \theta_D}{2})^2\right] \tag{16}$$

Where E_{LM} is the energy trace in momentum, E_{LAP} is the LEC for position limit in angle and the θ_D here stands for the angle detected on the detector.

Lastly, their model introduced a scaling factor for the photoemission intensity, which is a Jacobian to account for the coordinate transformation from angle to momentum. By applying this scaling factor, the conversion process ensures the photoemission intensity reflects the true intensity distribution of electronic states within the material.

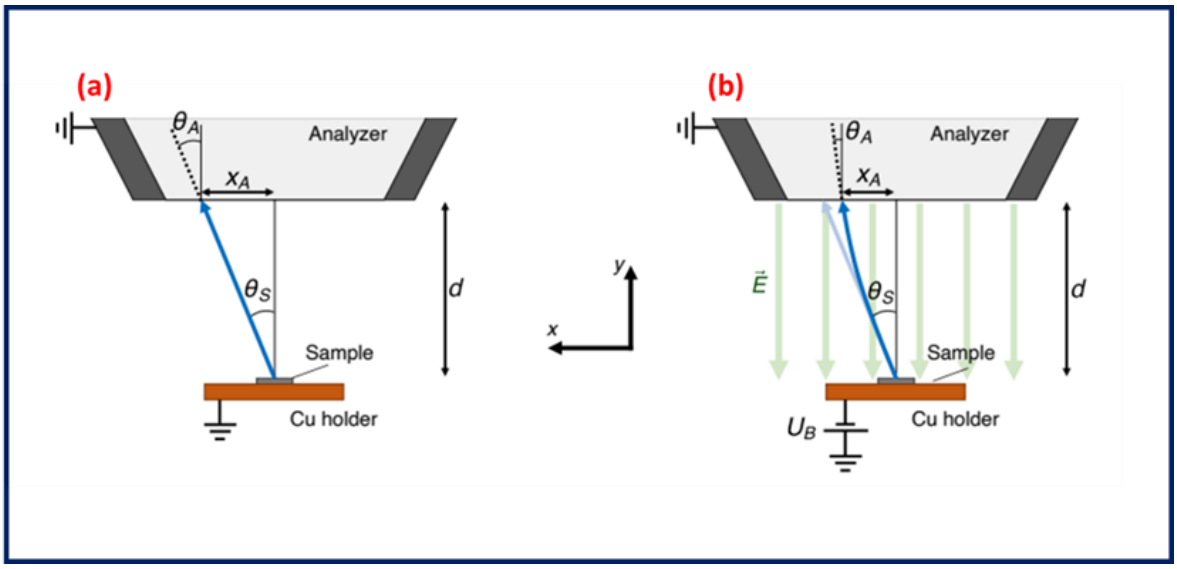

Figure 2. 1: Electron trajectories in an ARPES setup with a hemispherical analyzer. (a), without bias voltage, electrons emitted at an angle θ_s follow straight trajectories, and their transverse position x_A at the analyzer is determined by the emission angle $\theta_A = \theta_s$ (b), with an applied bias voltage U_B the electric field bends the trajectories, reducing θ_A and x_A allowing the detection of electrons emitted at larger angles, effectively expanding the momentum field of view[10]

The extended model

Although the above model was robust and adequately justified the results, it only addressed the emission angle along the slit direction, as this was a limitation of the ARPES setup used in that work. Therefore, their model was not applicable for systems equipped with the new deflector technology in ARPES setups. While an angle-to-momentum conversion model for an ARPES system using a deflector lens system has been developed in Ref. [29], it did not account for systems applying voltage to the sample. Furthermore, their geometric calculations were based on an assumption that holds true only for small emission angles accepted by the analyzer entrance. As a result, it was necessary to rederive these angle-to-momentum conversion equations, specifically for systems with sample bias, to improve accuracy.

Additionally, the position limit, which fitted the data in Ref. [10], did not fit our measured data at the Advanced Laser Light Source (ALLS) laboratory. Specifically, E_{LAP} overestimated our measured ARPES spectrum. To address this discrepancy, we derived a new expression based on the parabolic relationship in angle, considering the angular limit (E_{LAA}):

$$E_{LAA} = -\frac{eU_B^*}{(cos\theta)^2} \tag{17}$$

However, this expression underestimated our measured ARPES spectrum, as illustrated in Figure 2.2.

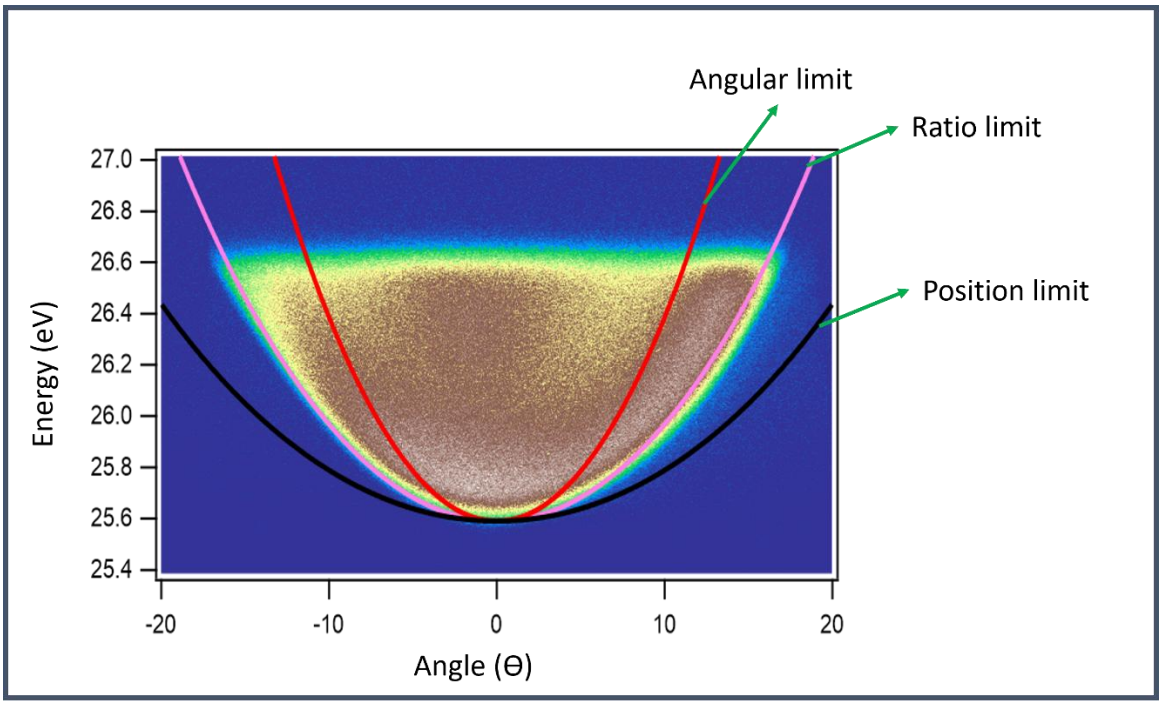

Figure 2. 2: Comparison of Angular, Position, and Ratio Limits in Angle-to-Momentum Conversion: This image illustrates the three limits proposed for converting angles to momentum in ARPES experiments under varying bias conditions. The angular limit (red parabola) assumes that the angle at the detector (ϑ) is identical to the angle at the analyzer entrance (θ_A), following a conventional approach. However, this model tends to overestimate the detected momentum. The position limit (black parabola) focuses on the position of electrons at the entrance of the analyzer, considering the bending effect of the electric field between the sample and the analyzer. This model, however, underestimates the momentum coverage. The ratio limit (RL) (pink parabola) represents a balanced approach, incorporating contributions from both angular and positional limits.

It is important to note that the lens column used in Ref. [10] did not include the octupole deflector, which is present in the system used in our experiment. Given the complex design of the ASTRAOIS lens column, this difference could be a significant reason why neither the position nor angular limits fit our measured data accurately. However, it can be expected that, whenever the LEC parabola accurately fit the angular data, a reasonable conversion from angle to momentum is obtained.

Based on this, we developed a method to adjust the measured cutoff to the expected LEC parabola. We consider an intermediary case between the position and angular limits, which we refer to as the Ratio Limit (RL) for the purposes of this work. By incorporating contributions from both limits, represented as a (for the position contribution) and b (for the angular contribution), the RL allows for a balanced adjustment that can be fine-tuned to different samples and experimental conditions to fit an ideal parabolic shape. These contributions are complementary, such that their sum is equal to 1 (a+b=1), leading to:

$$RL = (a * (E_{LAP} - E_{LAA}) + E_{LAA}) \tag{18}$$

From there, we extended the scaling factor for the position limit (F_{xy}) while that of angular limit is F, to include both momentum directions. For the detected angle along the slit direction k_x, we refer to it as θ_x, and for the detected angle in the k_y direction, as θ_y. Since the angular limit scaling factor does not depend on specific angles, it remains unchanged. We then modified Equations 1 and 2 to incorporate the RL scaling factors for both k_x and k_y directions.

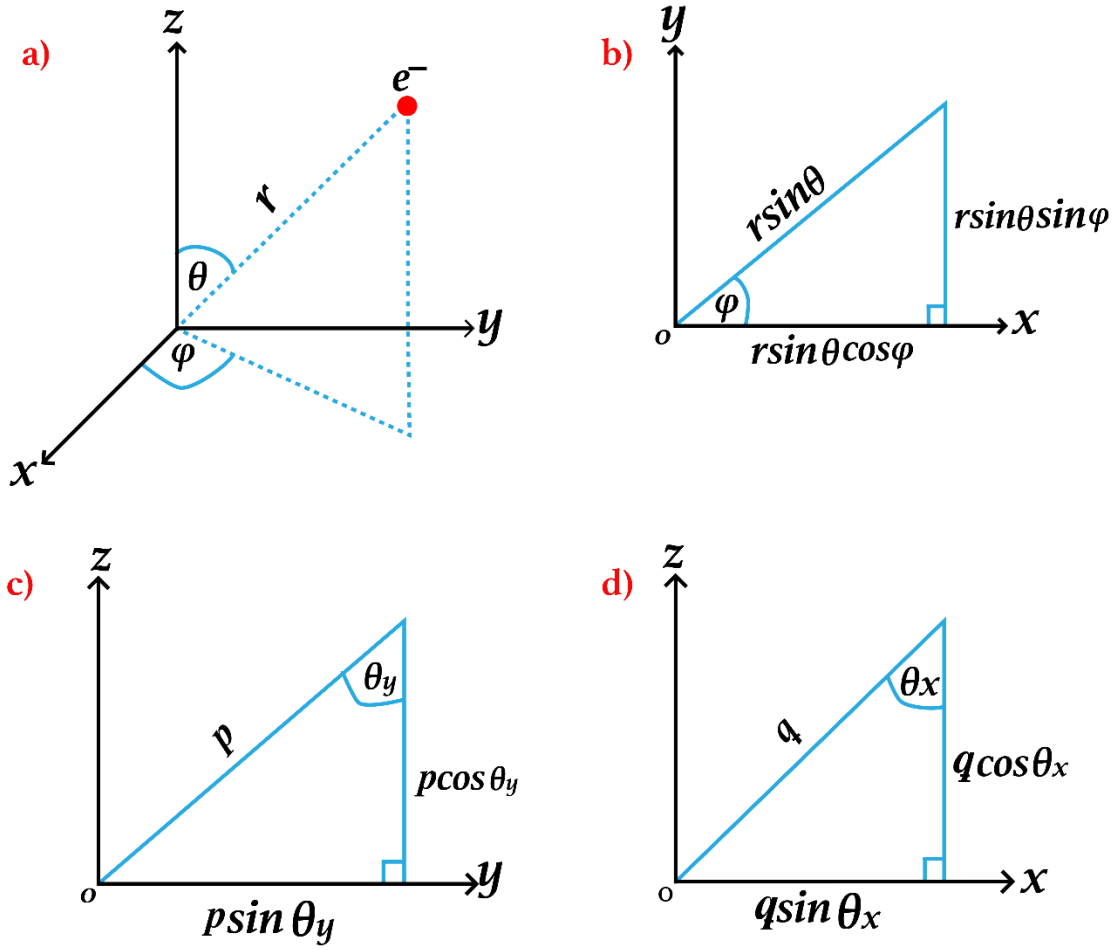

Figure 2. 3: (a) Represents the 3D Cartesian coordinate system (x, y, z) with an electron positioned in space, where θ and φ define the spherical coordinates. (b) Shows the projection of the electron into the XY plane with resultant vectors $r\ sin\theta sin\varphi$ and $r\ sin\theta cos\varphi$ (c) Depicts the projection into the YZ plane, with the angle θ_y determining the components $pcos\theta_y$ and $psin\theta_y$. (d) Shows the projection into the XZ plane, where θ_x defines the components $qcos\theta_x$ and $q\ sin\theta_x$

Now considering the 3D cartesian in figure 2.3 with an electron in the x-y-z coordinates, we can project the particle position into the XY, XZ and YZ plane and establish relations to the emission angle components θ_x and θ_y.

$$qsin\theta_x = rsin\theta cos\varphi \tag{19}$$

$$psin\theta_y = rsin\theta sin\varphi \tag{20}$$

$$qcos\theta_x = rcos\theta = pcos\theta_y \tag{21}$$

Using trigonometry and algebra we can deduce the following relations from the above expressions:

$$tan\theta_x = tan\theta cos\varphi \tag{22}$$

$$tan\theta_y = tan\theta cos\varphi \tag{23}$$

$$tan\varphi = \frac{tan\theta_y}{tan\theta_x} \tag{24}$$

$$tan\theta = \sqrt{tan^2\theta_x + tan^2\theta_y} \tag{25}$$

$$sin\theta cos\varphi = \frac{tan\theta_x}{\sqrt{1 + tan^2\theta_x + tan^2\theta_y}} \tag{26}$$

$$sin\theta sin\varphi = \frac{tan\theta_x}{\sqrt{1 + tan^2\theta_x + tan^2\theta_y}} \tag{27}$$

Hence:

$$F_{xy} = \sqrt{\frac{\alpha + 1 + \sqrt{2\alpha + 1 - \alpha^2\left(tan^2\theta_x + tan^2\theta_y\right)}}{2}} \tag{28}$$

$$k_x = \frac{1}{\hbar}\sqrt{2mE_k} \times F_{RL} \times \frac{tan\theta_x}{\sqrt{1 + tan^2\theta_x + tan^2\theta_y}} \tag{29}$$

$$k_y = \frac{1}{\hbar}\sqrt{2mE_k} \times F_{RL} \times \frac{tan\theta_y}{\sqrt{1 + tan^2\theta_x + tan^2\theta_y}} \tag{30}$$

$$F_{RL} = \left(a * F_{xy}\right) + (1 - a) * F \tag{31}$$

The final aspect of the model that was extended involved the intensity correction. The existing model already included an intensity correction to account for the angular dependence of the detected photoemission signal, ensuring that the intensity was accurately represented when converting from angle to momentum space. However, this correction is one dimensional and does not account for when analyzing a Fermi surface, which requires consideration of the entire 2D momentum space. To extend the intensity correction for application to a Fermi surface, we employed a Jacobian transformation. The Jacobian is a mathematical tool that provides the necessary correction factor when transforming between coordinate systems—in this case, from angular coordinates ($I(\theta_x, \theta_y)$) to momentum coordinates ($I\left(k_x, k_y\right)$). The Jacobian determinant accounts for the change in area when moving from the angular space to momentum space, ensuring that the intensity is scaled correctly across the entire Fermi surface.

$$I\left(k_x, k_y\right) = I\left(\theta_x, \theta_y\right) \cdot \left|\det\left(J\left(k_x, k_y\right)\right)\right|^{-1} \tag{32}$$

$$\det\left(J\left(k_x, k_y\right)\right) = \frac{\partial k_x}{\partial \theta_x} \cdot \frac{\partial k_y}{\partial \theta_y} - \frac{\partial k_x}{\partial \theta_y} \cdot \frac{\partial k_y}{\partial \theta_x} \tag{33}$$

Chapter Three: Materials and Experimental Procedure

Instrumentation

All instrumentation used in this study were provided by the TR-ARPES endstation at the ALLS laboratory in Varennes, Quebec.

Laser System: The photon energy used for the study was a 6 eV probe, generated from a 50 W Yb:YAG laser source with a wavelength of 1030 nm. This was achieved using non-linear crystals (BBO), which doubled the frequency to 515 nm. The fundamental 1030 nm and 515 nm beams were summed to generate 343 nm, and finally, the 515 nm and 343 nm beams were summed to produce 206 nm (6 eV)[30]. The beam spot size for these measurements was approximately 70 microns.

ARPES System: The 6-eV beam is directed to the ARPES chamber onto the sample stage. The ARPES system used for this work is a SPECS-designed system with a hemispherical analyzer called the ASTRAIOS that has an acceptance angle of 60 degrees for photoemitted electrons, utilizing deflector technology. Due to this technology, the system has three detection modes namely the Medium Angle Mode (MAM) which has acceptance of 20 degrees, the Wide-Angle Mode (WAM) which has an acceptance of 40 degrees and the Super Wide-Angle Mode (SWAM) with an acceptance angle of 60 degrees.

The analysis and preparation chambers maintained base pressures of $< 10^{-10}$ mbar. Sputtering and annealing cycles of Au(111) were performed in the preparation chamber, which is equipped with a sputter gun and an electron-beam heater. The analysis chamber is also equipped with an electron-beam heater.

Voltage Source: The bias voltage was generated from a DC power supply source by Hewlett Packard, model 6228B, and connected to the ARPES system with a BNC cable through the electron-beam heater connector, which is directly connected to the sample holder to increase the temperature in the analysis chamber during measurements. This setup is illustrated in Figure 3.1. However, this line for the e-beam heater also serves as the grounding line for the sample, which is why we can apply voltage through this mechanism.

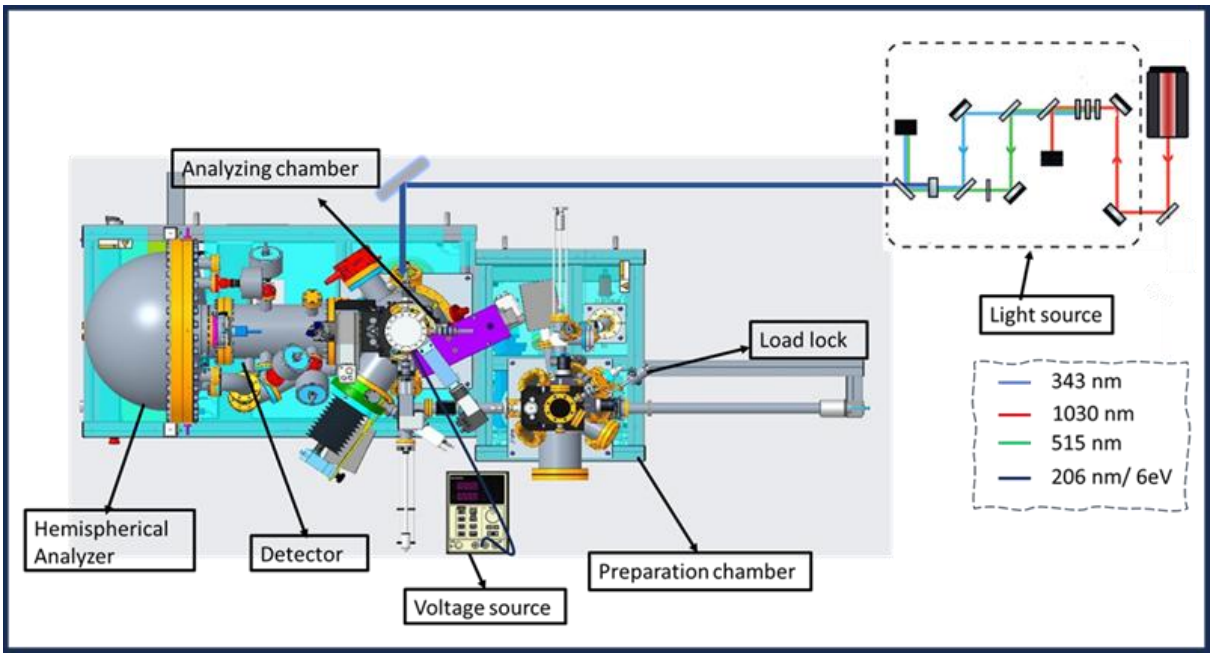

Figure 3. 1: A schematic of the experimental setup from the light source to the ARPES system.

Materials and preparation

Au(111)

The main material for this study is Au(111), chosen for its well-defined and sharp surface state[31], [32], [33]. Its clear Fermi level and surface states provide a reliable reference for comparing results under varying experimental conditions. The Au(111) sample was prepared by sputtering and annealing cycles in the preparation chamber. It was sputtered for 30 minutes with Ar^+ ions, followed by annealing. The temperature was gradually increased from room temperature to 900 K and then gradually decreased back to room temperature. The annealing process took about 30 minutes, achieved by increasing the current in the electron-beam heater from 2 mA to 18 mA and vice versa.

Other materials

WTe_2: The electronic structure of 1T-WTe_2 is highly anisotropic, meaning that the electronic dispersion varies significantly depending on the crystallographic direction. This makes it ideal to study the electronic structure for both slit directions for the different dispersions of its electronic structure when a bias is applied to see which of the directions provides a sharper dispersion[34], [35]. To prepare the sample for measurement a ceramic top-post was glued to the surface with silver epoxy and cured at 110°C for one

hour. The sample was then cleaved on the sample manipulator under a pressure of < 10^{-10} mbar at a temperature of approximately 10 K.

$Bi_2Sr_2CaCu_2O_{8+\delta}$ (Bi2212): Bi2212, a high-T_c cuprate superconductor, is renowned for its Fermi surface dominated by CuO_2 planes, its strong electron correlations, and the presence of a pseudogap, which are critical for understanding its unconventional superconductivity [3], [36], [37], [38]. Additionally, the material exhibits band folding due to structural modulation along the b-axis, introducing replicas of the Fermi surface[39]. Applying a bias to Bi2212 during tr-ARPES experiments enables access to a significantly larger portion of momentum space in a single experimental shot, all while preserving the matrix elements. This expanded coverage allows for simultaneous investigation of the electronic dynamics near both the nodal and antinodal regions, offering a detailed view of the dynamic processes occurring in tr-ARPES experiments. Bi2212 was prepared the same way as WTe_2.

Sr_2RuO_4: Sr_2RuO_4, is a layered perovskite and unconventional superconductor, displays a distinctive four-fold symmetry in its Fermi surface, a characteristic of its tetragonal crystal structure[40], [41], [42]. This material also features a pronounced nesting effect, stemming from parallel sections of its Fermi surface[43]. However, these features are challenging to measure with low photon energy, such as 6 eV, due to the limited accessible momentum space. In this work, we apply bias to enhance electron collection, thereby accessing a larger momentum space. Specifically, we aim to characterize any distortions or deviations from the expected four-fold symmetry and nesting effects that may arise as a consequence of the applied bias.

Experimental Details: Au(111)

Experiments with the three detectors modes were performed on Au(111) to select the most suitable mode for the experiments. Voltage dependence measurements were performed on Au(111) with voltages ranging from -5 V to -30 V. This was done to estimate the momentum coverage as bias voltage increases. From this we also find the trend on how the energy and momentum features are being affected for different bias for both slit directions. The work function of the analyzer was also determined to be 4.45 eV using equation 1. These measurements were performed at a temperature of 10K and a pass energy of 10eV.

Slit dependence test was also done on Au(111) for slits with width from 0.1mm to 1mm. A bias voltage of -30V was used and a pass energy of 10eV. These were measured at a temperature of 30K. These

measurements were done to determine how the slit width affects the angular resolution especially in the transverse momentum with bias.

Flux dependence studies were also performed. For all measurements, except those related to flux dependence, the beam flux was kept constant. In flux dependence studies, the count rate per second, as recorded by the detector, was used as the unit of measurement. This measurement was done for bias voltages, -30V, -10V and -6V. A pass energy of 4eV was used. This measurement was performed as part of space-charge studies to identify any nonlinearities or artifacts that may occur at higher flux levels. These include potential energy and momentum broadening under different bias conditions.

Experimental Details: other materials

Voltage dependence experiments were performed on the WTe_2. For WTe_2 bias voltages ranging from -15 V to -35V were used at a pass energy of 20eV at 298K. This was also done to see the momentum coverage as bias voltage increases.

For Bi2212 and Sr_2RuO_4 measurement were performed to ascertain the momentum coverage with bias using -35V and -90V respectively.

Chapter Four: Analysis on Au(111)

Detector modes

In Chapter 3, we introduced and defined the three detector modes—SWAM, WAM, and MAM—which are used in the ARPES system we used for the experiment. Now, we proceed to compare how these modes perform in the presence of applied bias voltages and analyze their effectiveness. To determine the most suitable detector mode for analyzing the effects of bias voltage, we plotted the measured dispersion in angle and traced the LEC in angle for both the slit direction and the transverse slit direction. A bias voltage of -35 V and a pass energy of 20 eV were used for these measurements.

From Figure 4.1, the top row (panels a, c, and e) represents the slit direction (θ_y), while the bottom row (panels b, d, and f) represents the direction transverse to the slit (θ_x). Examining the SWAM mode (panels a and b), we observe the contributions for the angular limit and the position limit are different. In the θ_y direction, the contributions are evenly distributed, whereas in the θ_x direction, the position limit contributes 20%. Additionally, this mode is very sensitive to alignment and hence very difficult to align.

In the WAM mode both the θ_y (c) and the θ_x (d) directions demonstrate the same contributions for both limits with a position limit contribution of 75%. The spectrum, in this case, fills a larger portion of the detector, covering about two-thirds, with no visible loss or truncation in the spectrum. This expanded coverage on the detector ensures fine details in the spectrum are easily resolved without significant compromise.

In contrast, the MAM mode (Figures e and f) shows a dominant contribution from the position limit in both directions. Although this mode allows the spectrum to cover the most substantial portion of the detector compared to the other modes, it fails to capture the full spectrum. Significant portions of the spectrum are truncated on both sides, indicating that not all electrons are effectively collected.

Comparing the three modes, we chose the WAM mode for several reasons. First, it provides consistent contributions from both the angular and position limits across all directions. Second, the WAM mode offers more efficient alignment and avoids the challenges encountered with the SWAM mode, which can be difficult to align consistently. The WAM mode meets this criterion more effectively than the SWAM and MAM modes. The SWAM mode's alignment issues and sensitivity make it less reliable, while the MAM

mode requires much higher voltages to collect all emitted electrons, which can degrade resolution over time. Therefore, the WAM mode represents the optimal choice for bias-dependent ARPES measurements.

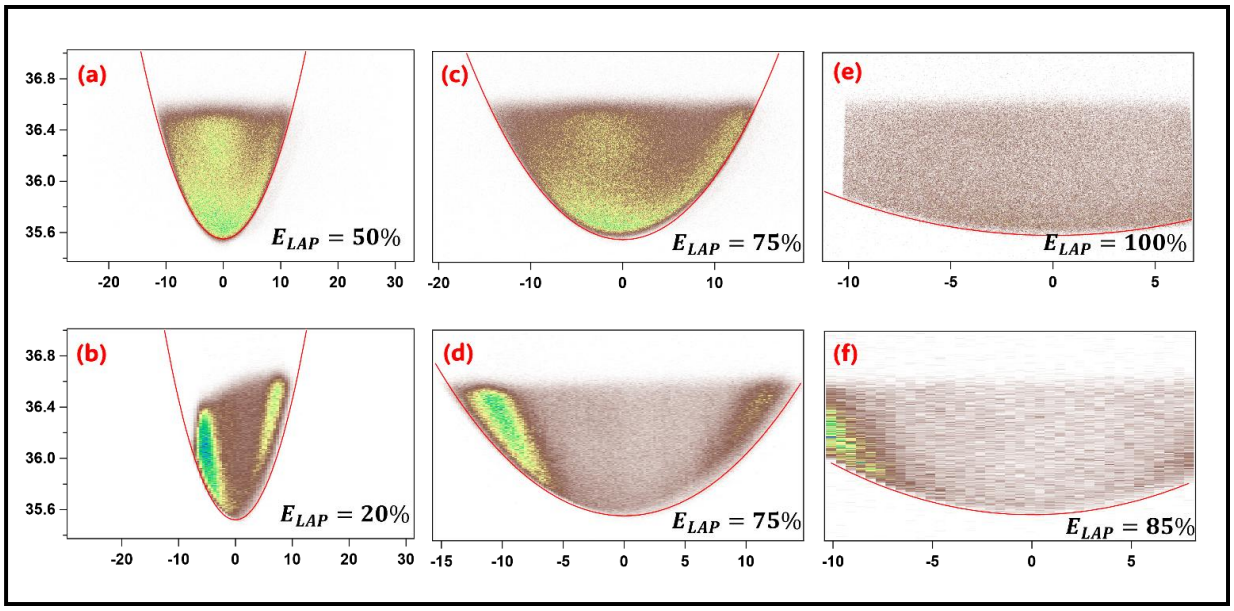

Figure 4. 1: Comparison of the measured dispersion in angle and the traced low-energy cutoff (LEC) parabola for the in-plane slit direction (top row: a, c, e) and the out-of-plane slit direction (bottom row: b, d, f) across three detector modes: SWAM (a, b), WAM (c, d), and MAM (e, f).

Angle to Momentum conversion.

In Chapter 2, we established that the accuracy of the angular-to-momentum conversion in reference [10] is validated when the low-energy cutoff (LEC) accurately fits the dispersion parabola in angle. To assess this accuracy, we first determine the conversion using the Ratio Limit/intermediate position. For these measurements, we used Au(111), which was sputtered and annealed to ensure sharp surface state bands. The raw data, obtained in angular space, is plotted against the sample's kinetic energy, as shown in Figure 4.2.

Figures 4.2a-4.2d represent the θ_y direction, with bias voltages of -30V, -20V, -10V, and -5V, respectively. Figures 4.2e-4.2h show the θ_x directions, with the same bias voltage order: -30V, -20V, -10V, and -5V, from top to bottom. The LEC is fitted to the data as the red parabola overlaid on the plots.

In both directions, the LEC trace fits the data well, demonstrating the effectiveness of the Ratio Limit approach. The position limit (ELAP) contributes 81% in the θ_y direction and 85% in the θ_x direction which was constant for all voltages. Using the same parameters, we then calculated the conversion from angle to momentum.

This conversion is demonstrated in Figure 4.3, where the momentum-space data is overlaid with the low-energy cutoff. The converted data fits well with the LEC in both momentum directions, confirming that both the angular and positional limits contribute when bias is applied to our system for Au(111). However, the difference in contributions between the two directions likely arises due to the geometric configuration of our lens system and potentially the alignment of the sample.

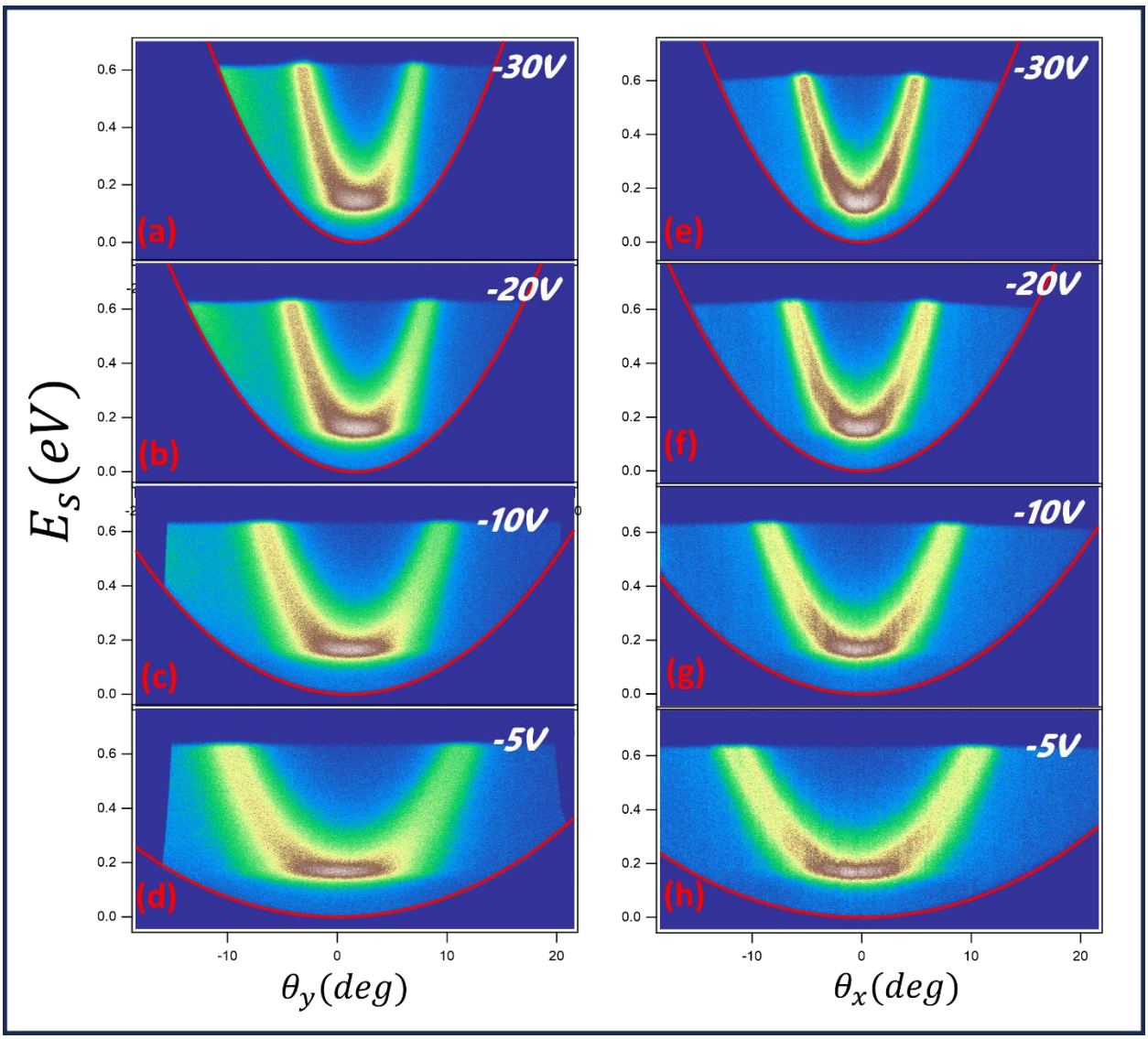

Figure 4. 2: Angular measurements of photoemitted electrons from Au(111) at different bias voltages. Panels (a) to (d) show the data for the slit direction at bias voltages of -30V, -20V, -10V, and -5V, respectively. Panels (e) to (h) show the data for the transverse slit direction, with the same bias voltages in the same order. The red parabola represents the fitted low-energy cutoff (LEC) trace, which is used to analyze the contributions from the angular and position limits in the momentum conversion.

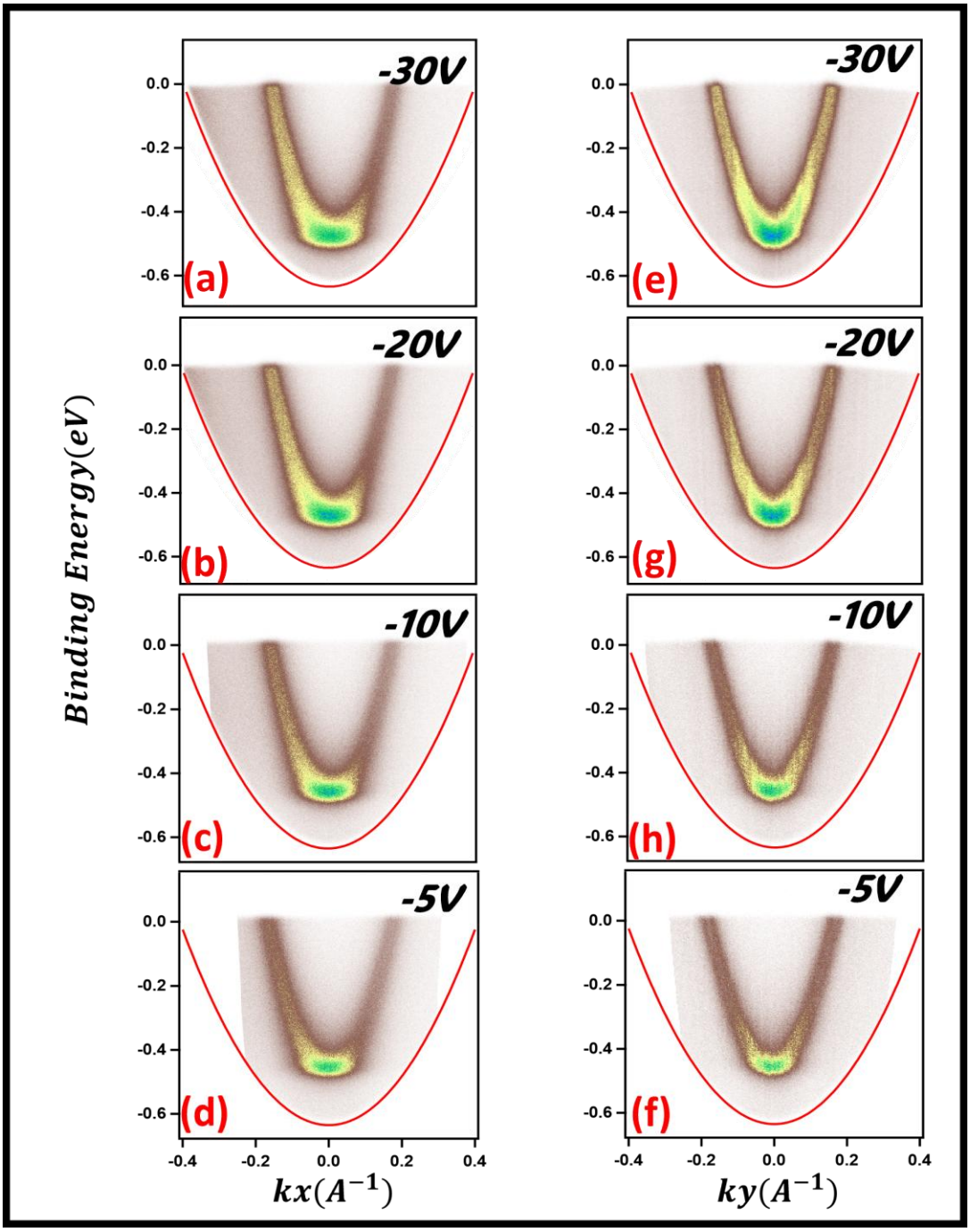

Figure 4. 3: Angle-to-momentum conversion for Au(111) overlaid with the low-energy cutoff in momentum space. Panels (a-d) represent the conversion of the θ_y direction from Figure 4.2, while panels (e-h) show the conversion of the θ_x direction from Figure 4.2 The red curves represent the fitted low-energy cutoff.

Angle to Momentum conversion (fermi surface).

Next, we measured the Fermi surface of Au(111) and converted the data from angular space to momentum space using the same parameters for the limits as before (81% for the θ_y direction and 85% for the θ_x direction in terms of position limit). This is shown in Figure 4.4. Panels a-d represent the measured data in angular space, where we observe that lower bias voltages (-5V) occupy a larger area of the detector compared to higher bias values, as expected from the predictions made in Chapter 2. As the bias voltage decreases, the photoemitted electrons spread over a larger angular range, and the corresponding momentum coverage increases as well. This can be attributed to the reduced focusing effect at lower bias, which leads to less electrons been collected from wider emitted angles. Panels 4.4e-h show the converted angle-to-momentum data, where the momentum coverage increases as the bias voltage increases (from -5V to -30V). A larger bias voltage helps collect more photoemitted electrons, leading to a more extended region in momentum space. This observation validates our earlier predictions regarding the expansion of the momentum range under higher bias voltages, as discussed in Chapter 2, where it was noted that applying bias would effectively "fold" the electron trajectories, increasing the momentum coverage without rotating the sample.

Figures 4.4i and 4.4j represent the converted data for -30V and -5V, respectively. Both figures are overlaid with a red circle, which marks the low-energy cutoff (LEC) in momentum space. This overlaid circle highlights the boundary of the momentum space that can be accessed given the photon energy of 6 eV, taking the sample's work function to 5.39 eV. The work function was estimated by subtracting the difference between the Fermi level and the lowest point of the LEC paraboloid from the photon energy. In this case, the 6 eV photon energy can cover a momentum radius of approximately 0.4 $Å^{-1}$, which provides an upper bound for the accessible momentum space in our measurements.

From Figure 4.3 and Figures 4.4e-h, we observe that the features of the converted data are consistently aligned, and the momentum positions remain in the same locations, confirming the robustness of the conversion process. To validate our angle-to-momentum conversion data, we compared the surface state ring—represented by the circular ring in the data—with reported values from the literature. Our data yields a ring diameter of 0.34 $Å^{-1}$, which is in good agreement with the values reported by other researchers: 0.33 $Å^{-1}$[31], 0.34 $Å^{-1}$ [44], [45], and 0.36 $Å^{-1}$ [46] in various studies. This confirmation of the surface state ring's position adds credibility to our momentum mapping process. The diameter we report here corresponds to the average of the outer and inner surface state ring in Au(111). Au(111) is known to exhibit two surface state rings: an inner and an outer circle. The observation of only a single ring in our

data may be attributed to two possible factors. First, the sample was not sufficiently sputtered and annealed during the cleaning process, resulting in significant impurity scattering. This leads to broad spectral features, preventing the resolution of the two bands. Secondly, hydrogen may have condensed onto the sample surface, as the measurement was conducted below the hydrogen condensation temperature (~30 K), potentially obscuring the surface state ring.

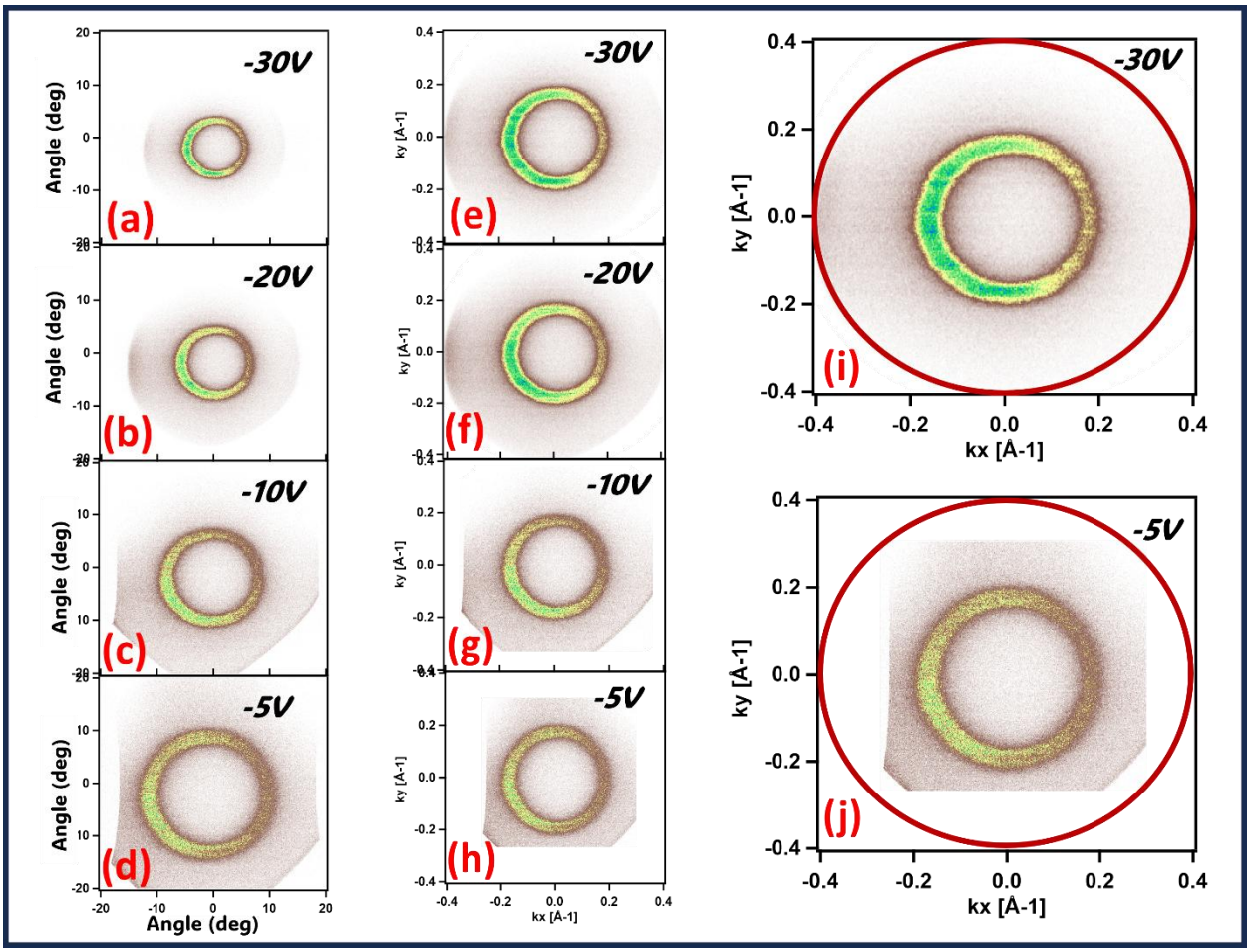

Figure 4. 4: Fermi surface measurements of Au(111) at different bias voltages, converted from angular to momentum space. Panels (a-d) show the measured data in angular space for bias voltages of -30V, -20V, -10V, and -5V. Panels (e-h) show the converted data, with higher bias voltages resulting in broader momentum coverage. Panels (i) and (j) display the converted data for -30V and -5V, overlaid with the red circle representing the low-energy cutoff (LEC) in momentum space. The measured surface state ring diameter of 0.34 $Å^{-1}$ agrees with literature values, validating the conversion method.

Effects of applied Bias on the Energy Axis

To investigate how varying bias voltages influence the energy axis, Energy Distribution Curve (EDC) analysis was conducted on the photoemission data. In this analysis, the bands in the negative and positive momenta were analyzed independently. The Fermi edge was fitted to a Fermi-Dirac distribution function, which was convoluted with a Gaussian resolution function. The resulting position of the Fermi level and the full width at half maximum (FWHM) of the resolution function were extracted from the fit. The FWHM reflects the energy broadening at the Fermi level. This process was repeated for both momentum directions, kx and ky, to assess any directional dependence of energy broadening. The energy axis was then normalized to the kinetic energy available at the surface of the sample, as defined by Equation 9.

In Figures 4.5a and 4.5b, the energy resolution changes by less than 2 meV across varying bias voltages in both momentum directions. This indicates that although some broadening occurs, it remains relatively small and consistent. It can therefore be concluded that the effect of bias voltage on energy broadening is minimal in both emission directions. This minimal broadening is consistent with findings reported in reference [10], supporting the notion that the applied bias does not significantly perturb the intrinsic energy axis in either direction.

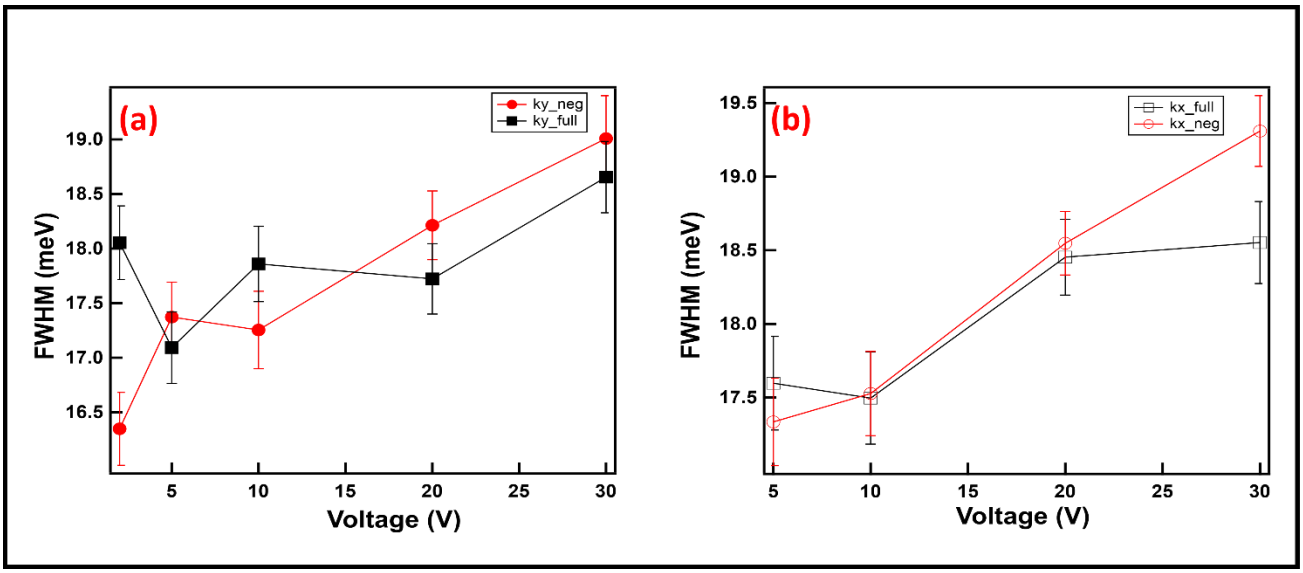

Figure 4. 5: Energy distribution curve (EDC) analysis for Au(111). Panels (a) and (b) show the corresponding full width at half maximum (FWHM) as a function of bias voltage for kx and ky, representing the energy resolution at different bias levels. The variation in FWHM with bias voltage reflects the influence of the applied electric field on the electronic structure and the energy distribution.

Effects of applied Bias on the Momentum Axis

To investigate the effect of the applied bias on the momentum axis, momentum distribution cuts (MDCs) were taken from the converted Fermi surfaces in Figure 4.4e-h for both ky (θ_x) and kx (θ_y). These MDCs are presented in Figure 4.6, where 4.6a corresponds to ky and 4.6b corresponds to kx.

Upon visual inspection, we observe that in ky, which represents θ_x direction, at lower applied voltage values, there are two distinct peaks on either side of the momentum axis. These peaks represent the two wavevectors characteristic of a Rashba-split system in Au(111). In contrast, in the kx direction, which corresponds to the θ_y direction, both wavevectors are indistinguishable due to poor resolution. At first glance, this suggests that the θ_x direction has a better resolution θ_y direction. However, this conclusion should be taken with caution, as the overall quality of the sample, as mentioned earlier, may influence the results, making a definitive conclusion difficult at this stage.

To further investigate this, we performed another set of MDCs at 0.48 eV below the Fermi level for both kx and ky momentum directions, shown in Figure 4.7b and 4.7c, respectively. The MDCs were fitted with Gaussian functions, and the FWHM was extracted to quantify the angular spread. The dependence of FWHM on the applied bias voltage is illustrated in Figure 4.7a.

As shown in Figure 4.7a, the FWHM increases as the bias voltage rises, indicating that the angular spread of the photoemitted electrons broadens under higher bias conditions. This result confirms our prediction in Chapter 2. However, a notable difference appears when comparing the FWHM for ky and kx. In Figure 4.6a, we can see that the FWHM for ky is lower compared to kx, suggesting that the angular resolution in the θ_x direction (ky) is slightly better than in the θ_y direction (kx).

This broadening in momentum, reflected in the increased FWHM, indicates that while higher bias voltages improve the collection of photoemitted electrons, they also reduce the momentum resolution. However, as predicted, the reduction in momentum resolution is minimal and does not significantly impact the overall momentum resolution, especially in the θ_x direction (ky).

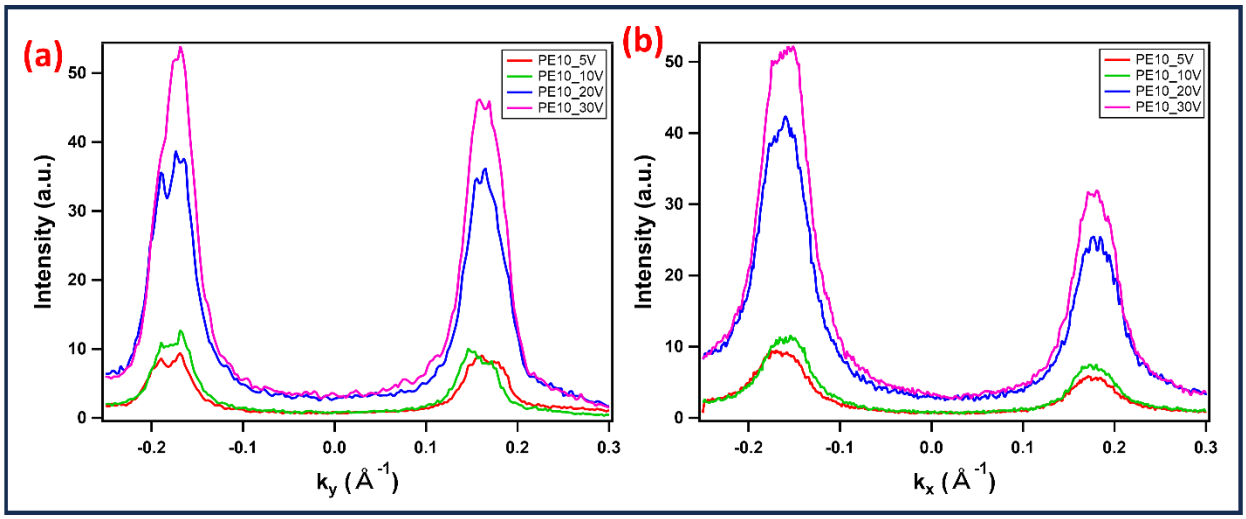

Figure 4. 6: Momentum distribution cuts taken from the converted Fermi surfaces in Figure 13e-f: (a) for the ky direction (out-of-plane slit) and (b) for the kx direction (in-plane slit). The MDCs are plotted for various bias voltages, showing the effect of increasing bias on the angular spread and the broadening of the peaks

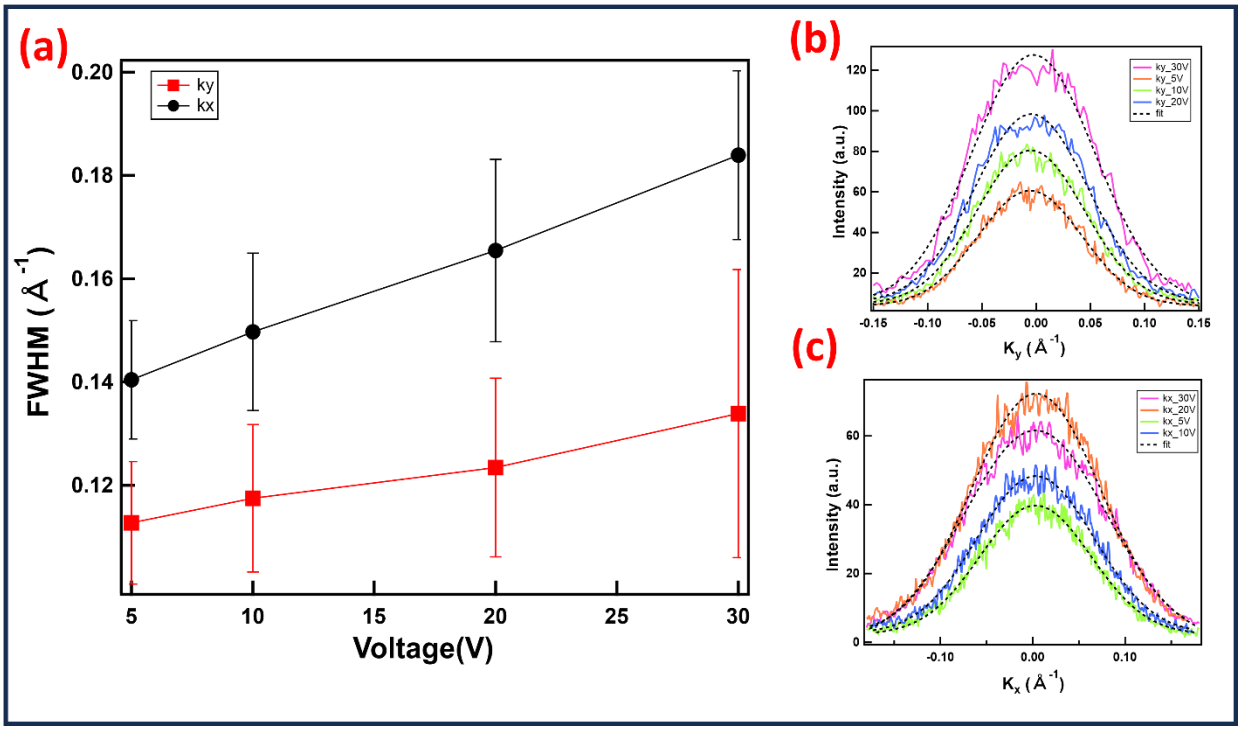

Figure 4. 7: FWHM from momentum distribution curves (MDC) at 0.48 eV from Figure 12 for kx (black circles) and ky (red squares) directions. The plot shows how the FWHM increases with bias voltage, indicating a broadening of the momentum distribution at higher bias. Panels (b) and (c) display the MDC cuts at 0.48 eV for kx and ky directions respectively, across bias voltages (-30V, -20V, -10V, and -5V). The increasing width of the peaks with higher bias demonstrates the broadening effect of bias on the momentum distribution.

Effects of applied bias voltage on analyzer slit.

In Chapter 1, we discussed the significance of the entrance slit of the analyzer (fixed aperture) and how, as shown in Equation 7, the energy resolution of the experiment is directly proportional to the slit width. This factor is also crucial for the angular resolution. In this section, we examine the effects of the applied bias on both slit directions for the energy axis and momentum axis.

These studies were performed with a bias voltage of -30V. The sample was re-prepared and measurements were conducted at 30 K, above the condensation temperature of hydrogen, to ensure clearer observation of the Au(111) surface state. This is illustrated in Figure 4.8, which presents the Fermi surfaces for six different slit widths, ranging from 1 mm to 0.1 mm. We begin by analyzing how the slit width affects the energy axis.

To assess this, we fitted the Fermi level using a Fermi-Dirac distribution convoluted with a Gaussian function, integrating the data from the positive branch to the negative branch for both directions (kx and ky). As shown in Figure 4.9b, we observe a steady Fermi level as the slit width increases, with a slight shift at the largest slit width. This shift is unexpected and might be attributed to the unique design of the ASTRIAOS slit system, which is positioned slightly away from the entrance of the analyzer, unlike conventional hemispherical analyzers where the slit is directly at the entrance. Additionally, slight changes in sample alignment or detector calibration may also contribute to this effect.

In Figure 4.9a, we see that as the slit width increases, the FWHM of the energy peak also increases. The relationship between slit width and energy resolution is well-established in photoelectron spectroscopy and is demonstrated in Equation 7. The entrance slit controls the range of emission angles accepted by the analyzer, which directly influences the energy dispersion of the detected electrons. A narrower slit allows only a small range of angles to pass through, resulting in better energy resolution as the electrons are more precisely focused. However, as the slit width increases, a broader range of angles is accepted, leading to a greater angular spread and an increase in FWHM.

Although we observe a change in FWHM shift with varying slit widths, the applied bias voltage has minimal effect on these parameters in the energy axis. From the data, the changes in the energy resolution and Fermi level are more closely related to the slit width and the geometry of the slit system than to the applied bias voltage.

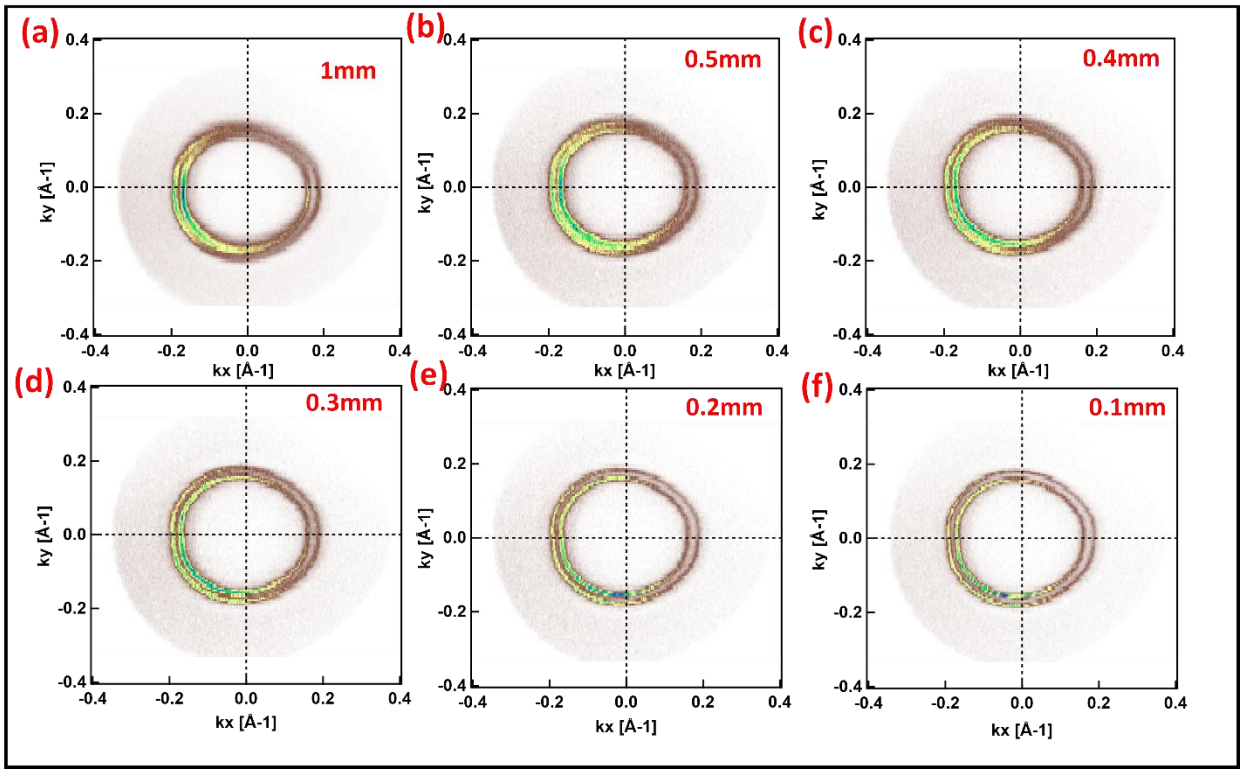

Figure 4. 8: Fermi surface mapping of Au(111) at -30V for various slit widths. Panels (a-f) show the Fermi surface measured at slit widths of 1 mm, 0.5 mm, 0.4 mm, 0.3 mm, 0.2 mm, and 0.1 mm, respectively. As the slit width decreases, the momentum resolution improves, resulting in clearer and more distinct inner and outer electron pockets. The data illustrates how the choice of slit width affects the sharpness of the momentum features, with smaller slit widths providing better-defined momentum distributions.

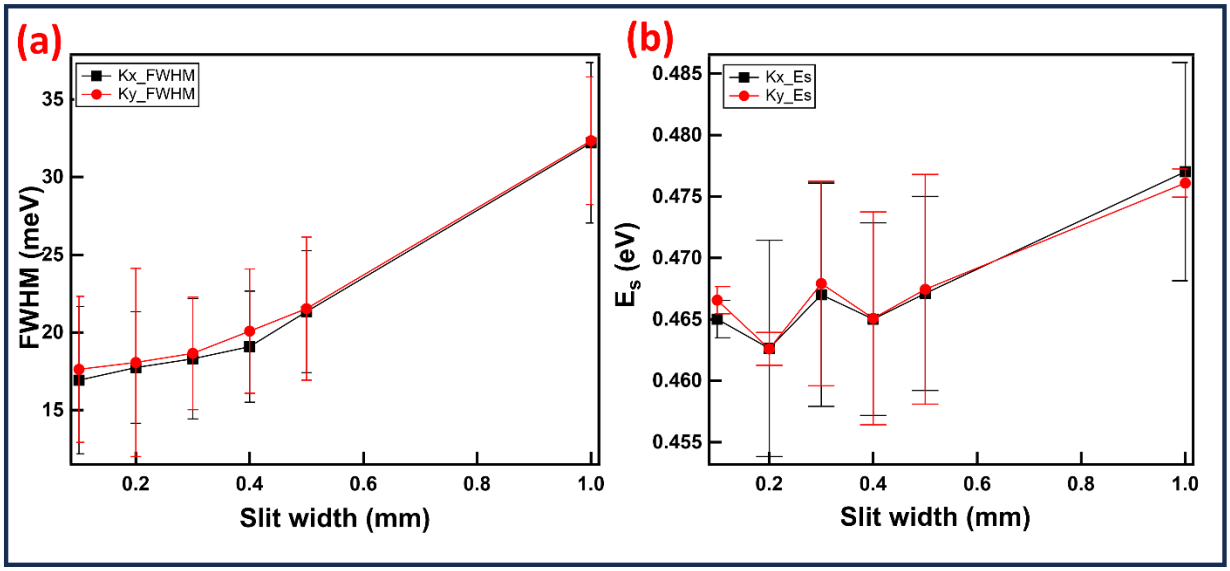

Figure 4. 9: Slit measurement graphs at -30V from Fermi-Dirac fits. (a) FWHM as a function of slit width for kx (black circles) and ky (red squares) directions, illustrating the broadening of the energy peaks as slit width increases, indicating reduced energy resolution at larger slit widths (b) Fermi level position as a function of slit width for kx (black circles) and ky (red squares) directions, showing how the Fermi level shifts with varying slit widths.

For the momentum axis, we refer to Figure 4.8. From the figure, it is evident that as the slit width is reduced, the inner and outer rings of the surface states become sharper and more distinct. In the ky direction, shown in panels a to c, we observe that the two rings appear to broaden and become less discernible as the slit width increases. This broadening is not as pronounced in the kx direction, where the slit is oriented in the in-plane direction. This suggests that the slit width has a more significant impact on the angular resolution in the ky direction (θ_x direction) than in the kx direction.

To gain a better understanding of this behavior, MDCs were taken at the dashed lines in Figure 4.8 and plotted in Figure 4.10. In Figure 4.10b, we can clearly see two distinct peaks for both the positive and negative momenta in the kx direction across all slit widths. This indicates that, regardless of slit width, the two peaks in the kx direction remain well-defined and maintain a high angular resolution.

However, in Figure 4.10a (the ky direction), the two distinct peaks in both the positive and negative momenta are only visible for slit widths ranging from 0.1 mm to 0.3 mm. For slit widths of 0.4 mm, 0.5 mm, and 1 mm, the peaks are no longer distinguishable, making it difficult to accurately measure the difference in peak positions. This loss of resolution at larger slit widths in the ky direction highlights the significant role of the slit geometry in defining the momentum resolution. As the slit width increases, a broader range of angles is accepted, leading to increased angular spread, which results in the broadening and eventual overlap of the two distinct peaks.

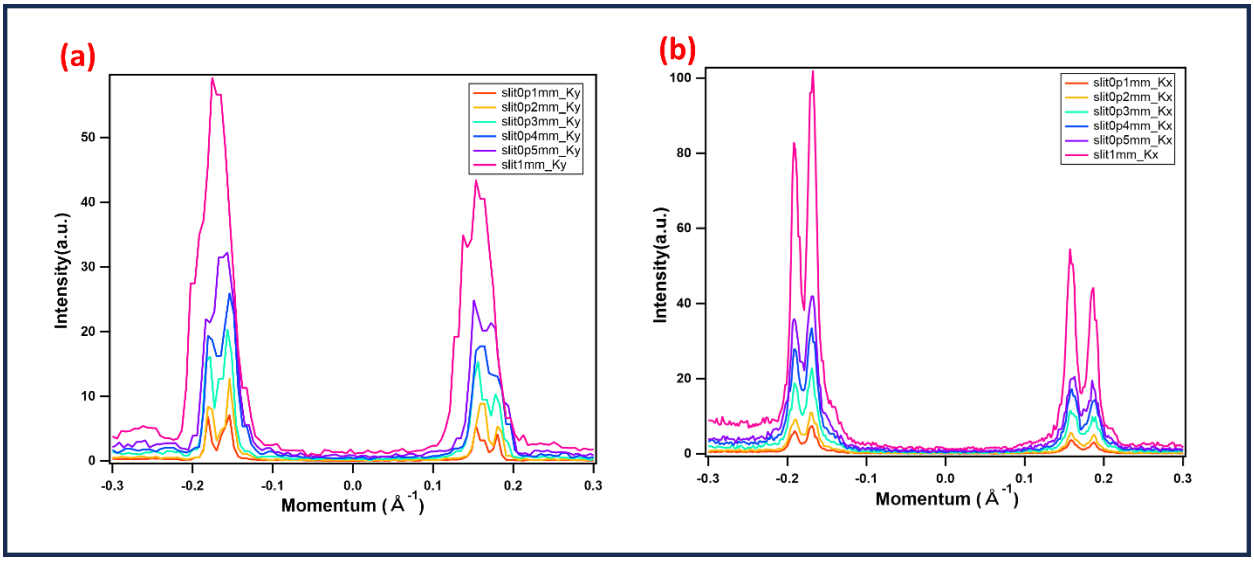

Figure 4. 10: MDC cuts taken along the dashed lines in Figure 8. Panel (a) shows the MDCs along the vertical dashed line (ky direction) and panel (b) shows the MDCs along the horizontal dashed line (kx direction)

The difference in peak positions is a well-studied parameter in Au(111) for Rashba studies, as it is directly proportional to the strength of the Rashba splitting. This splitting is a measure of the spin-orbit interaction strength in the material, which plays a crucial role in understanding the electronic structure and the material's potential applications in spintronic devices. Accurate extraction of the peak positions (Fermi vectors) and quantification of the Rashba splitting is essential for these studies.

To determine the peak positions, a double Lorentzian fit was applied to the MDCs. The peak positions for both positive and negative momenta in the kx and ky directions were extracted, and the differences in peak positions were calculated. As shown in Figure 4.11, the average change in peak position varies across all directions. In the negative kx direction, the change is approximately 0.0278 $Å^{-1}$, in positive kx it is 0.0221 $Å^{-1}$, in negative ky it is 0.0244 $Å^{-1}$, and in positive ky it is 0.0235 $Å^{-1}$. Given that Au(111) is expected to exhibit isotropic behavior (uniform spin-orbit interaction strength), any anisotropy in the observed Rashba splitting can be attributed to external factors, such as misalignment of the sample or inaccuracies in detector calibration.

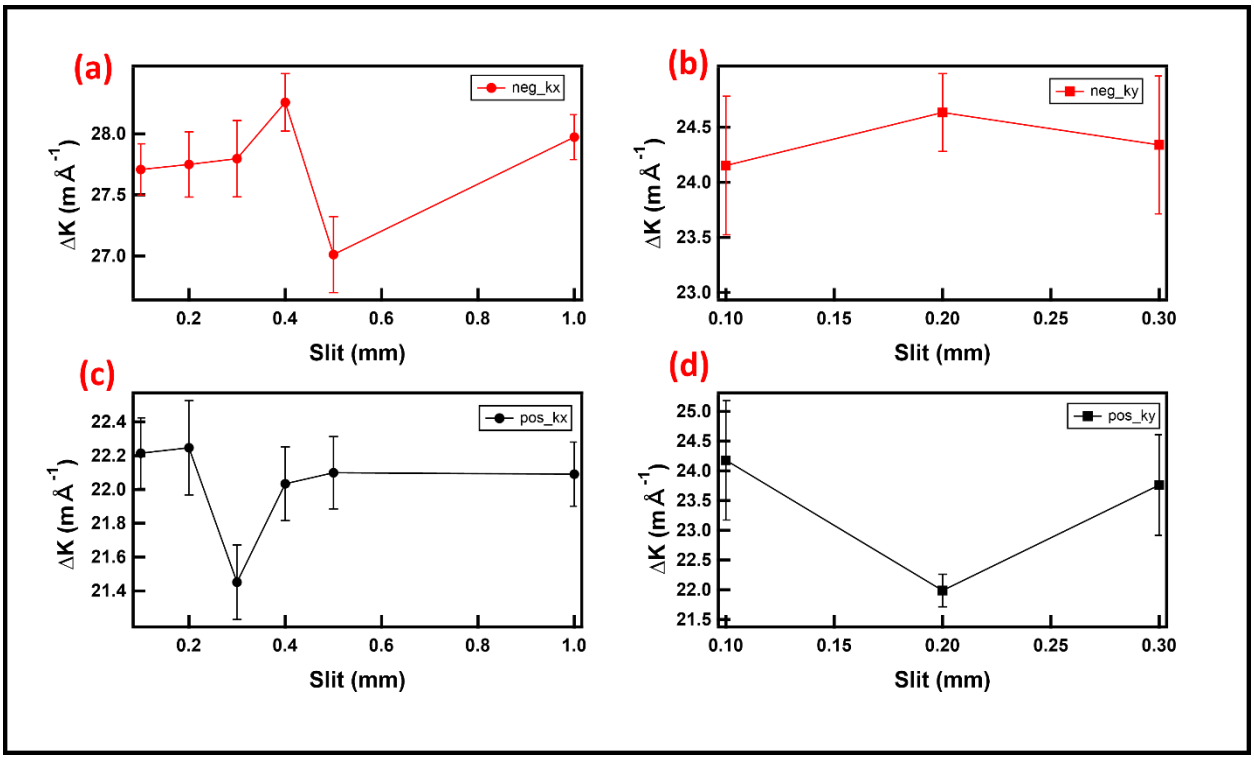

Figure 4. 11: Change in peak positions (Fermi vectors) for both kx and ky directions, measured for various slit widths. Panels (a) and (b) show the changes in peak positions for the negative kx and positive kx directions, respectively, while panels (c) and (d) show the changes for the negative ky and positive ky directions. The average change in peak position is calculated from the MDCs, with values corresponding to 0.0278 $Å^{-1}$, 0.0221 $Å^{-1}$, 0.0244 $Å^{-1}$, and 0.0235 $Å^{-1}$ for the respective directions.

The FWHM for the various peaks was also extracted to assess how sharp they were as the width of the slit changed. For this analysis, we focused on the kx momentum direction. As shown in Figure 4.12b, the FWHM increased as the slit width increased for all peak positions, except for the 1mm slit. The FWHM is a critical parameter that indicates the sharpness of spectral peaks, with narrower FWHM values corresponding to sharper, more well-defined peaks. As the slit width increases, the range of emission angles accepted by the analyzer also increases, leading to a broader angular distribution of detected electrons. This broader distribution results in a larger FWHM, reflecting a decrease in energy resolution and less sharply defined peaks. However, the exception observed with the 1mm slit is surprising and not understood and should be remeasured to confirm its validity.

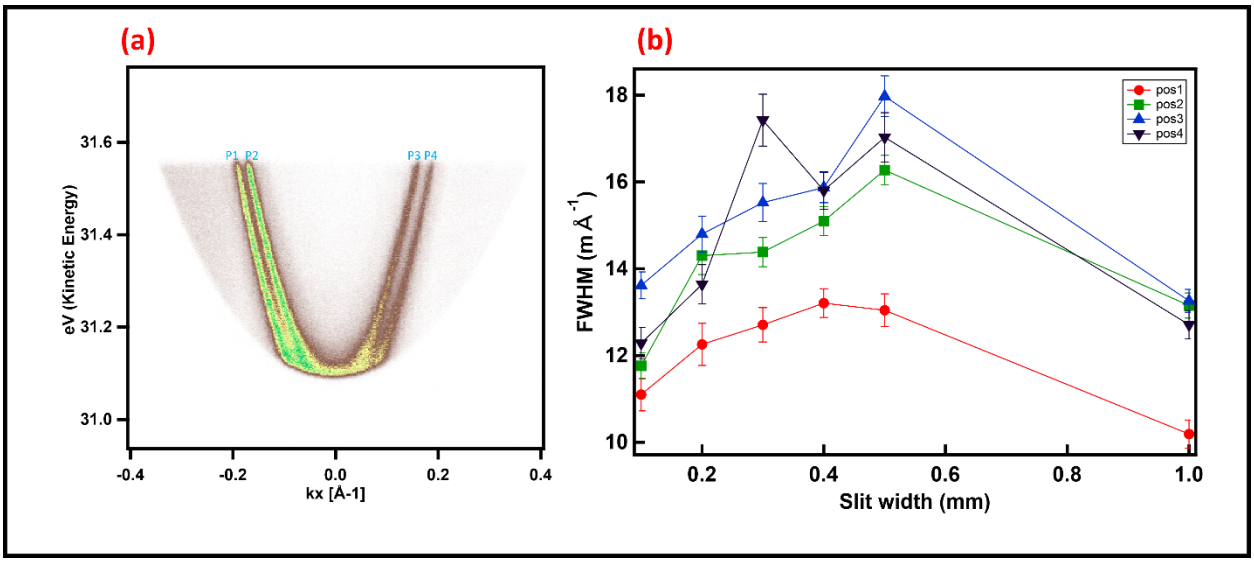

Figure 4. 12: Energy-momentum dispersion with positions P1-P4 (in light blue) indicating the Fermi vector positions chosen for analysis. (b) Full width at half maximum (FWHM) at the Fermi vector positions plotted against slit width. The data illustrates how the FWHM varies as a function of slit width at each of the four Fermi vector positions, demonstrating the impact of slit width on the momentum resolution.

Flux dependence.

For the flux dependence studies, measurements were conducted at three different bias voltages: 6V, 10V, and 30V, along the kx momentum direction. The flux was varied to check how space charge effects are modified with applying sample bias. At high flux, the increased number of photoelectrons can lead to a space charge buildup, which distorts the energy distribution of the emitted electrons. This effect can cause broadening of the peaks. For these measurements, the photon flux was fixed, and data was acquired for different voltage values. This procedure was repeated for various photon fluxes. Since the precision of the

voltage source is around 10 mV, the Fermi level position cannot be compared accurately in these measurements. Only the energy and momentum resolutions are investigated.

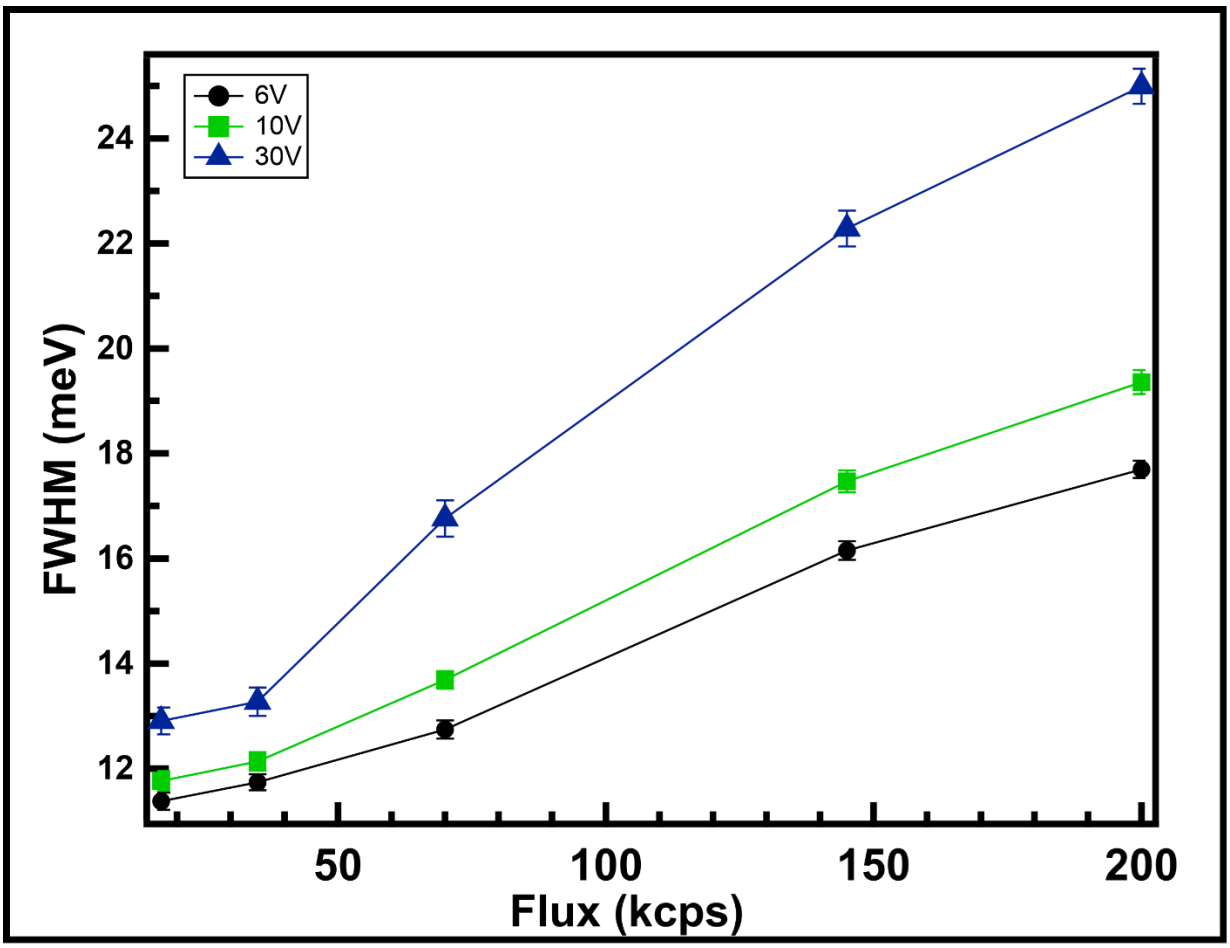

Figure 4. 13: Energy resolution (FWHM) plotted against flux intensity, demonstrating the broadening of the energy peaks as flux intensity increases for the different bias voltages.

In Figure 4.13, the FWHM is plotted against different flux values at various applied voltages. As the photon flux increases, we observe a corresponding increase in the FWHM. This trend is also reflected in Figure 4.15, where the FWHM values expand as the photon flux increases, indicating a reduction in the precision of the energy measurement.

The increase in FWHM with rising flux suggests that higher flux leads to broader energy distributions. This can be explained by the fact that a higher photon flux results in a greater number of photoelectrons being emitted. The larger number of electrons emitted causes the energy distribution to broaden due to space charge effects, and, therefore, an increase in the FWHM. Essentially, a higher photon flux means more

electrons are detected, but this also brings in a wider spread of energies, which results in a less defined energy peak.

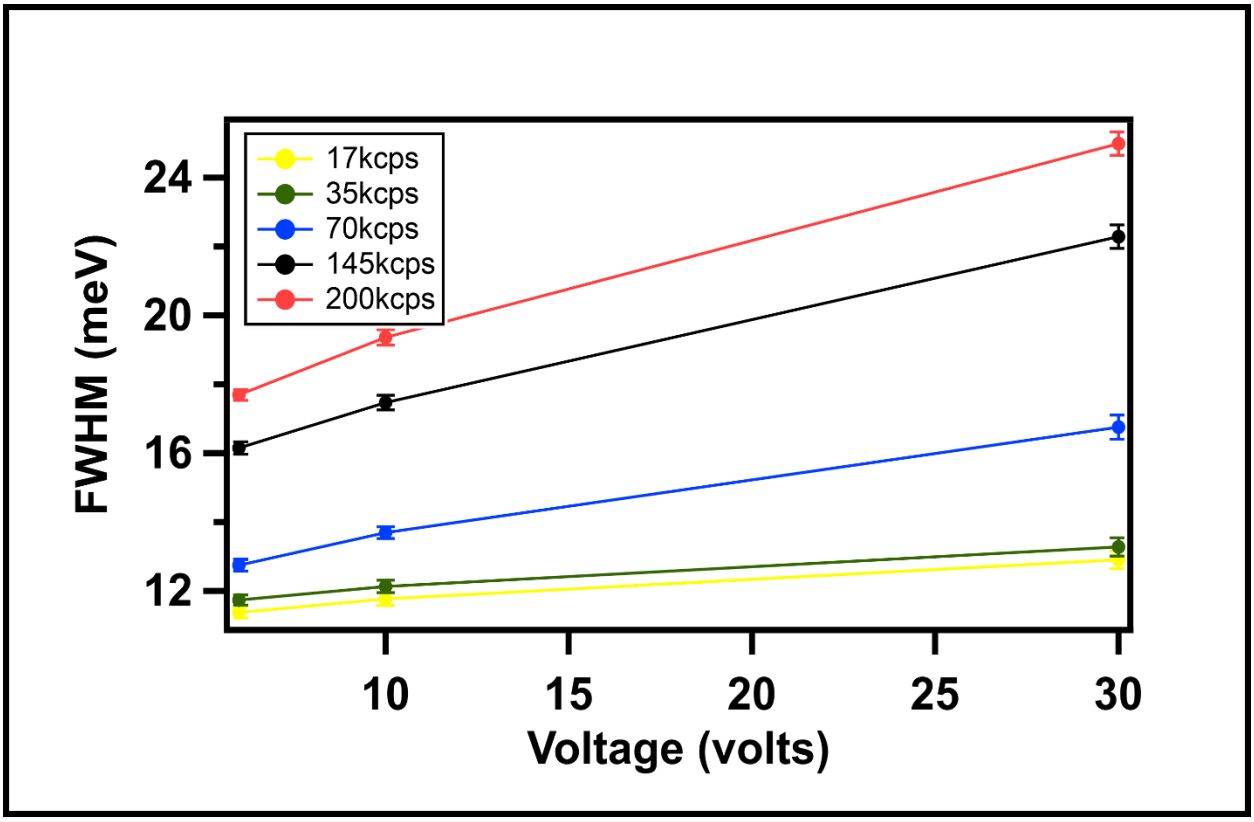

Figure 4. 14: Flux dependence of the FWHM. FWHM values for increasing photon fluxes: 17 kcps, 35 kcps, 70 kcps, 145 kcps, and 200 kcps . As the photon flux increases, the FWHM also increases, indicating a broadening of the energy distribution and a reduction in energy resolution

To analyze the angular distribution, we took a cut at 0.05 eV below the Fermi level, as indicated by the red line in Figure 4.15. At first glance, Figures 4.15c-d show that as the flux and bias voltages increase, the peaks broaden out. To gain a deeper understanding, double Lorentzian fits were applied to extract the offset in momentum. The broadening of peaks observed with increasing flux and bias voltage can be attributed to enhanced space charge effects. As the photon flux increases, more electrons are excited and emitted from the sample surface. These emitted electrons create an increasing electrostatic repulsion among themselves, known as space charge, which can cause the emitted electrons to spread out more in momentum space, leading to broader peaks.

The FWHM was extracted from the Lorentzian fits for both peaks in the MDCs, as shown in Figures 4.16b-c. For peak one, there is a gradual decline in the FWHM as the flux increases up to 145 kcps, followed by a sudden increase of about 20% at 200 kcps. For peak two, we see a steady decrease in FWHM for the 6V

and 10V bias voltages until the sudden increase after 145 kcps. However, for the 30V bias, the FWHM increases as the flux rises from 17 kcps to 145 kcps, followed by a sharp increase at 200 kcps. At lower flux values (17, 35, and 70 kcps), the gradual decline in FWHM for the 6V and 10V biases suggests that the momentum peaks become sharper as the flux increases, but this is likely due to reduced noise and fit quality as the change is comparable to the error bars. However, as the flux reaches 145 kcps, space charge effects begin to impact the momentum distribution. The sudden increase in FWHM at 200 kcps indicates that these space charge effects are broadening the momentum distribution, leading to less well-defined peaks. For the 30V bias, the initial increase in FWHM from 17 kcps to 145 kcps suggests that the higher bias voltage amplifies space charge effects earlier, causing greater momentum broadening even at lower flux levels. The sharp jump in FWHM at 200 kcps across all biases highlights the point at which space charge effects dominate, significantly reducing momentum resolution.

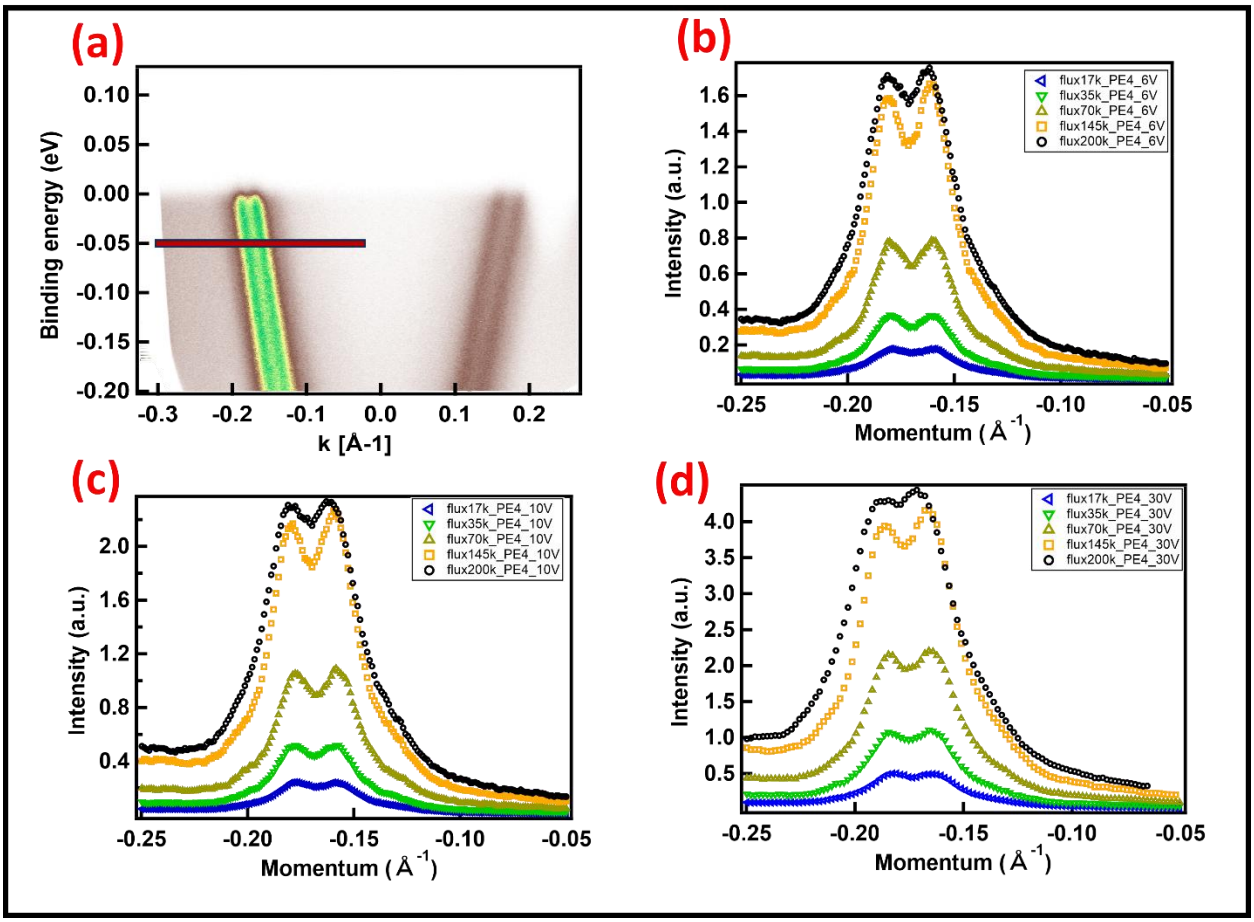

Figure 4. 15: Flux dependence studies from momentum distribution curves (MDCs) taken at 0.05 eV below the Fermi level, as indicated by the red line in panel (a). Panels (b-d) display the MDC plots for various flux intensities at different bias voltages: -6V (b), -10V (c), and -30V (d). The increasing flux intensities (17k, 35k, 70k, 145k, and 200k counts per second) lead to peak broadening in each plot, demonstrating how flux intensity impacts the resolution and momentum distribution across different bias conditions

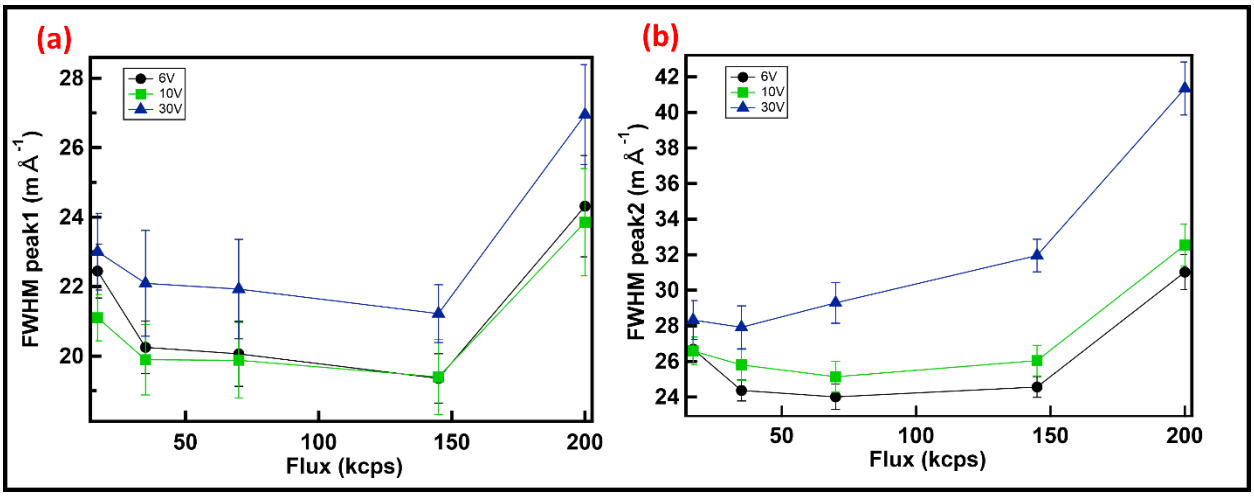

Figure 4. 16: Display the FWHM for the peak positions indicated in Figure 4.15, demonstrating how flux intensity impacts the broadening of the peaks at each bias voltage.

Challenges

Although applying bias voltage with our deflector technology expands the momentum field view and improves the signal-to-noise ratio, several challenges were encountered during the experiments that should be mentioned.

In Figure 4.8, visual inspection reveals that the two concentric rings, which represent the spin-orbit split Fermi surface of Au(111), do not appear as perfect circles, as expected. The non-circularity observed in the Fermi surface of Au(111) can be attributed to experimental issues such as alignment, and these effects might be further enhanced with the application of higher bias voltages (e.g., -30V in this case). Therefore, great care and time must be devoted to aligning the sample and fine-tuning experimental setups to minimize such distortions. A practical recommendation would be to consider using lower bias voltages when full momentum space coverage is not required, as this may help mitigate the observed issues.

Another challenge that became apparent during the experiment is the bending of the Fermi level with increasing photon flux. This is shown in Figure 4.17. The slit width used for panels (a-e) was 0.3 mm, and as the photon flux was doubled, the Fermi level shifted from a sharp, straight line to one that increasingly curved at the edges. This bending effect became more pronounced as the flux increased, and a tail started to form at the edges of the bands. In Figure 4.17f, where a wider slit of 0.5 mm was used, the same bending effect of the Fermi level was observed. The bending of the Fermi level observed in Figure 4.17 can be attributed to the space charge effect, which becomes more pronounced as the photon flux increases. As more photoelectrons are emitted due to higher flux, the electrostatic forces between the electrons distort

the trajectories of the electrons. This leads to a curving of the Fermi level and the formation of a tail at the edges of the bands.

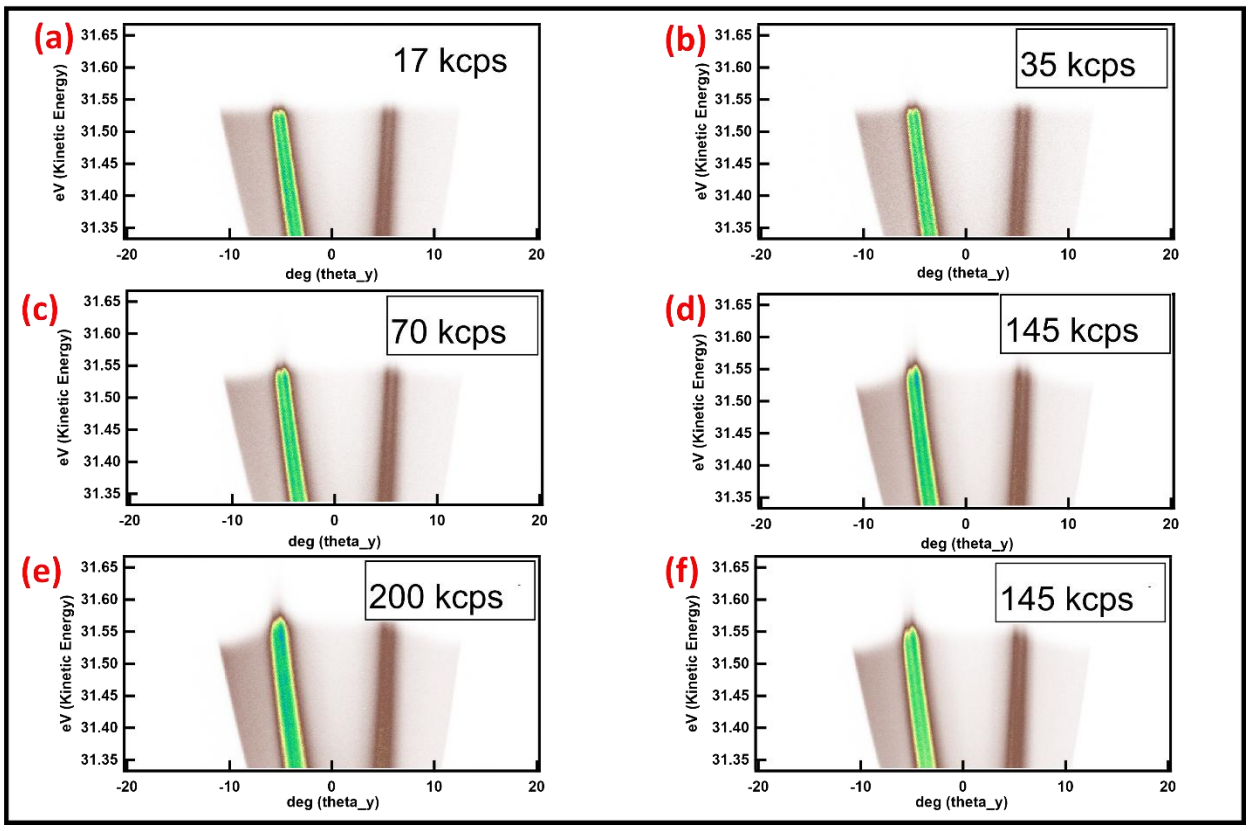

Figure 4. 17: Fermi level bending with increasing photon flux. Panels (a) to (e) show the Fermi level at different photon fluxes: (a) 17 kcps, (b) 35 kcps, (c) 70 kcps, (d) 145 kcps, and (e) 200 kcps, all measured with a slit width of 0.3 mm. The Fermi level progressively bends and develops a tail at higher fluxes, indicating the influence of space charge effects. Panel (f) shows the same bending behavior at 145 kcps with a wider slit (0.5 mm).

Chapter 5: Results on other samples

WTe_2

In this work, we mapped the Fermi surface of WTe_2 at bias voltages of -35V, -25V, and -15V, as shown in Figure 5.1. The sample was initially aligned at -35V to optimize the collection of photoemitted electrons. In this analysis, panels (a-c) show the raw data for these bias voltages, while panels (d-f) present the corresponding converted momentum images.

At -35V, we achieve the best momentum space coverage, allowing us to capture both electron pockets of the Fermi surface in full. The raw data in panel (a) clearly shows the two distinct electron pockets, and the corresponding momentum conversion in panel (d) confirms that these pockets are accurately represented in momentum space.

As we decrease the bias to -25V, we notice a reduction in the number of electrons captured by the analyzer. In panel (b), the electron pockets are still visible, but their intensity and clarity begin to fade. By the time we reach -15V, the reduction in bias voltage significantly limits the momentum coverage. Panel (c) clearly shows that at this lower voltage, the analyzer is no longer able to capture the full extent of the electron pockets, and the right side of the Fermi surface becomes harder to discern. This is further confirmed in panel (f), where only partial electron pockets are visible. The incomplete momentum coverage at -15V highlights the crucial role that bias voltage plays in determining how much momentum space can be accessed.

When we compare these results to the literature, particularly the study by Yang et al.[47], we find good agreement. In their work, the electron pockets of WTe_2 are observed at approximately ± 0.3 $Å^{-1}$ along the Γ-X direction, which matches well with the positioning of the electron pockets in our converted momentum images.

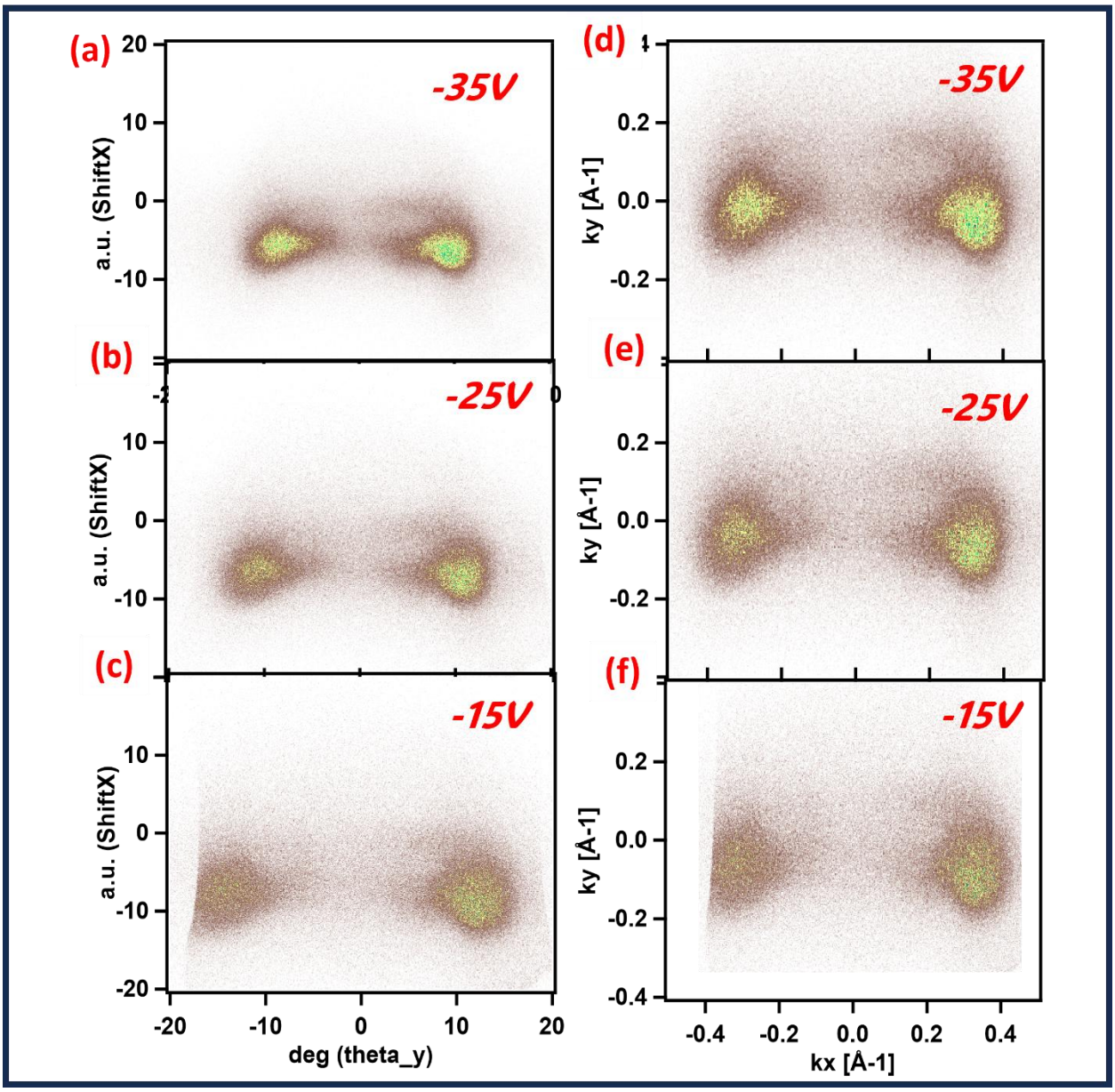

Figure 5. 1: Fermi surface of WTe_2 at different bias voltages. Panels (a) to (c) show the raw data acquired at bias voltages of -35V, -25V, and -15V, respectively. Panels (d) to (f) display the corresponding converted momentum images. At -35V, both electron pockets are clearly visible with optimal momentum coverage. As the bias voltage decreases to -25V and -15V, the electron pockets become less distinct, with reduced intensity and incomplete momentum coverage at -15V.

For the WTe_2 measurements, we also took into account the differing dispersions along the kx and ky directions. To assess this, we chose three different slit widths—0.1mm, 0.4mm, and 1mm—and used pass energies of 10eV for Γ-Y along kx and 3eV for Γ-X along kx. A bias voltage of -20V was applied throughout the experiment. The measurements for the Γ-Y along kx are presented in Figure 5.2.

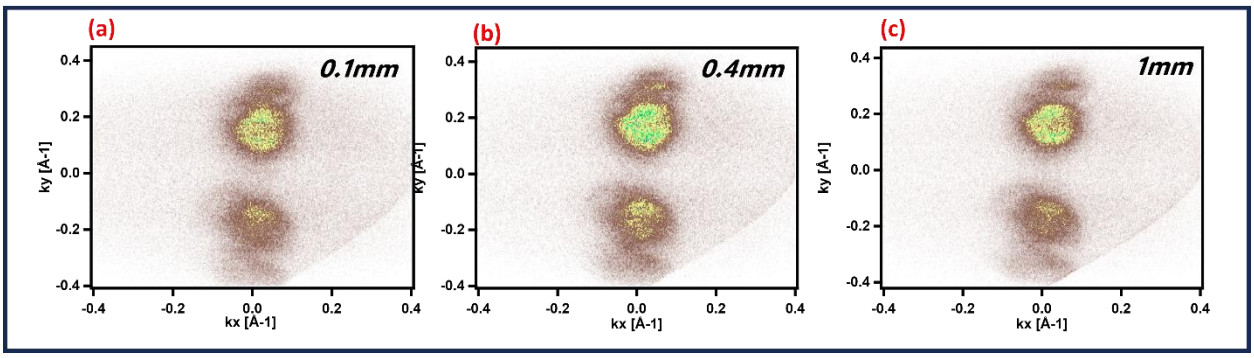

Figure 5. 2: Slit Dependence on WTe_2 Fermi Surface for the Γ-Y Direction along kx at Various Slit Widths. This figure illustrates the Fermi surface of WTe_2 for three different slit widths: (a) 0.1 mm, (b) 0.4 mm, and (c) 1 mm.

In Figure 5.3, we present measurements for the Γ-X direction along kx. Notably, the electron pockets in this direction are much more resolved compared to the ones of Figure 5.2. This improvement in resolution can be attributed to the lower pass energy used (3eV), as compared to the one used for Figure 5.2(10eV). It is well-established that using a lower pass energy improves the energy resolution of ARPES measurements, allowing for more precise detection of electronic states.

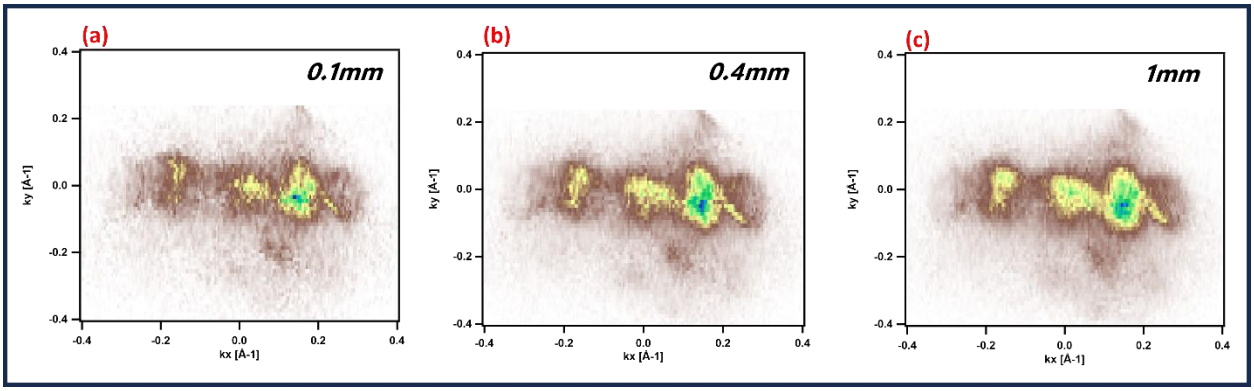

Figure 5. 3: Slit Dependence on WTe_2 Fermi Surface for the Γ-X Direction along kx. This figure presents the Fermi surface of WTe_2 for three different slit widths: (a) 0.1 mm, (b) 0.4 mm, and (c) 1 mm, measured with a pass energy of 3 eV. The data shows that the electron pockets are more resolved compared to Figure 5.2, likely due to the lower pass energy, which improves the resolution.

Sr_2RuO_4

This sample, Sr_2RuO_4, has previously only been studied with higher photon energies rather than using 6eV photons, suggesting that measuring its band structure with 6 eV is challenging. However, with our new sample biasing technique and deflector technology, we were able to collect the photoelectrons and map them onto the detector. As discussed in Chapter 2, to achieve good angle-to-momentum conversion, one

must ensure that the LEC parabola fits well with the data in angular space, considering the right contributions from both position and angular limits.

In Figure 5.4a, the ratio limit in red is fitted with the data in angle. We can see that the LEC fits the data to some extent. This tells us that the conversion in the momentum direction, θ_y will be acceptable. However, in Figure 5.4b-c, we see that we could not achieve a good ratio for the θ_x direction. The spectrum does not follow the expected parabolic dispersion.

For the above work, a pass energy of 20eV was used to ensure we could observe the lowest part of the parabola. Following this, measurements were taken at 10eV pass energy and bias voltages of 80V and 95V to see how the Fermi surface would look. This is presented in Figure 5.5, where we can see a clear distortion of the Fermi surfaces.

Though we were able to collect the electrons, it is not ideal to measure Sr_2RuO_4 with such techniques due to the distortions observed in the Fermi surface. The distortion is likely due to the low photon energy used in conjunction with the sample biasing and deflector setup, which doesn't allow for proper resolution and can cause unwanted effects on the electron trajectories. This makes the data less reliable for obtaining the true nature of the Fermi surface. For accurate measurements of materials like Sr_2RuO_4, it is better to use higher photon energies that can provide more efficient electron detection without such distortions.

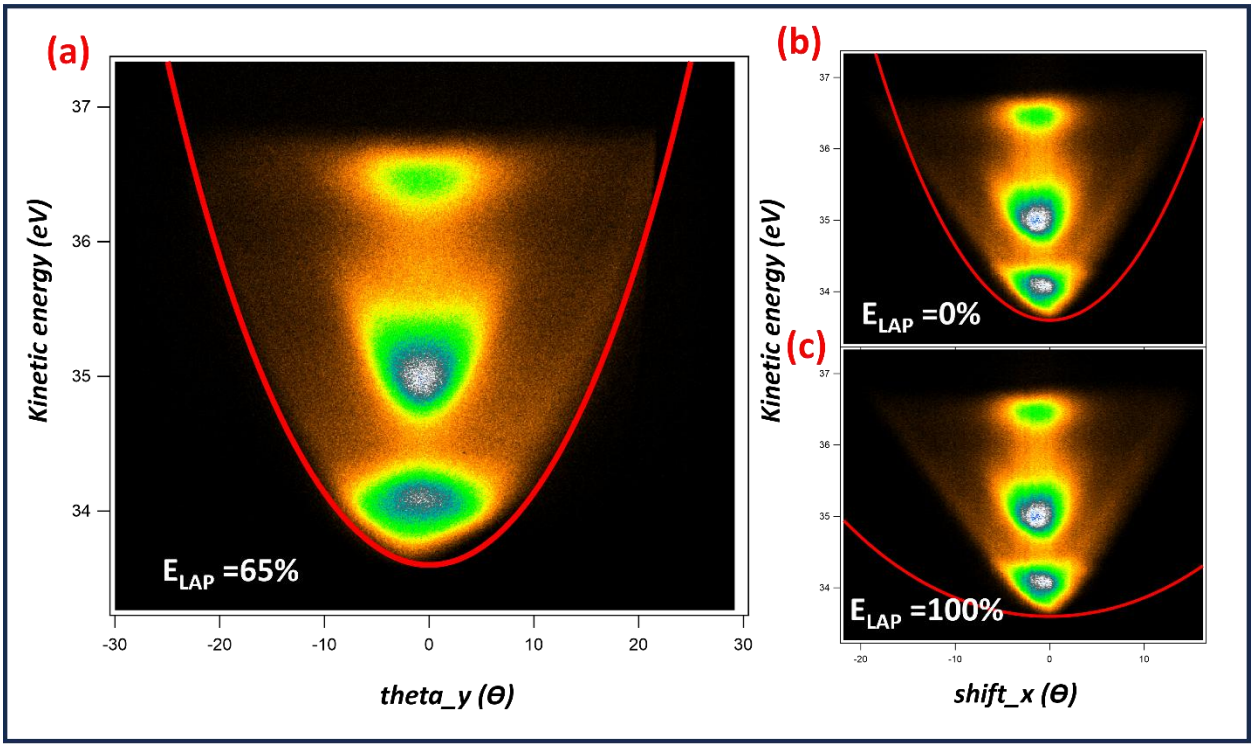

Figure 5. 4: ARPES Measurement of Sr_2RuO_4 a) Spectrum along the slit direction fitted with the ratio limit (red parabola), showing a 65% contribution from the position limit. (b) Spectrum along the direction transverse to the slit fitted with the red parabola using 100% angular limit. (c) Spectrum along the direction transverse to the slit fitted with the red parabola using 100% position limit.

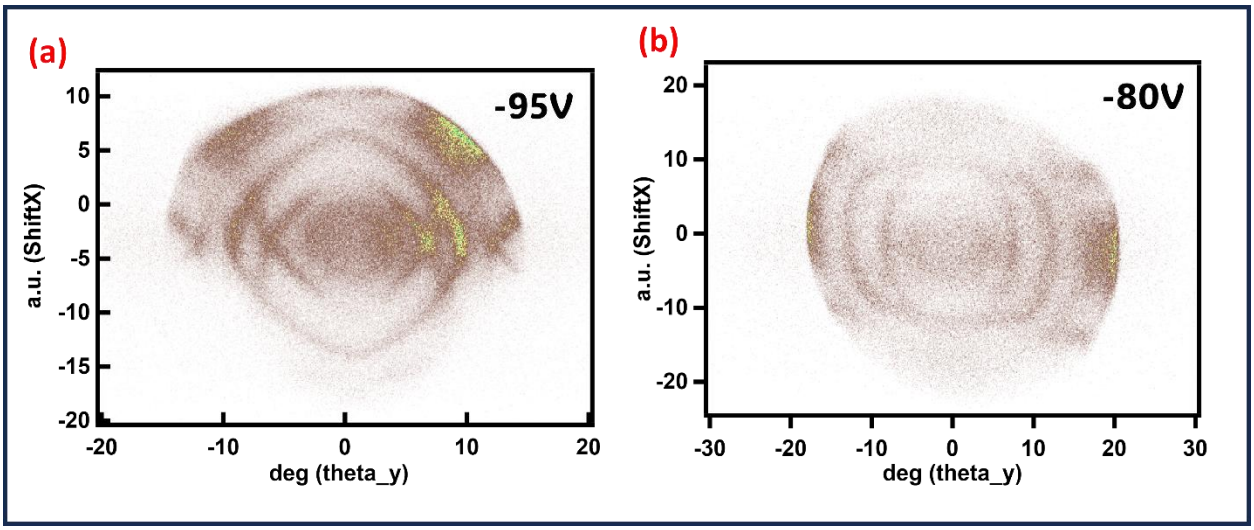

Figure 5. 5: Fermi Surface of Sr_2RuO_4 (a) Fermi surface measured at a bias voltage of -95V. (b) Fermi surface measured at a bias voltage of -80V.

Bi2212

With the new technology and sample biasing technique, we were able to acquire a clean and well-resolved Fermi surface of Bi2212, as shown in figure 5.6. This figure presents the Fermi surface of Bi2212 with four distinct arcs, all captured in a single ARPES experiment, without the need to rotate the sample. The red circle indicates the momentum reach, with a diameter of 0.72 $Å^{-1}$, which encompasses almost the entire Fermi surface in the kx-ky plane. This result is a notable improvement compared to previous studies on Sr_2RuO_4, as we achieved minimal distortion.

One of the key features captured here are the nodes and antinodes, which are critical for understanding the material's high-temperature superconductivity. The nodes represent regions where the energy gap is zero, while the antinodes correspond to areas where the gap is largest, and the superconducting pairing mechanism is most prominent. This ability to measure all four arcs simultaneously provides a comprehensive view of the Fermi surface, allowing us to study the complex interplay between these features in a single experimental setup.

This achievement marks a significant leap in the characterization of materials like Bi2212, as the ARPES measurements were previously limited by the need to rotate the sample or perform multiple experiments.

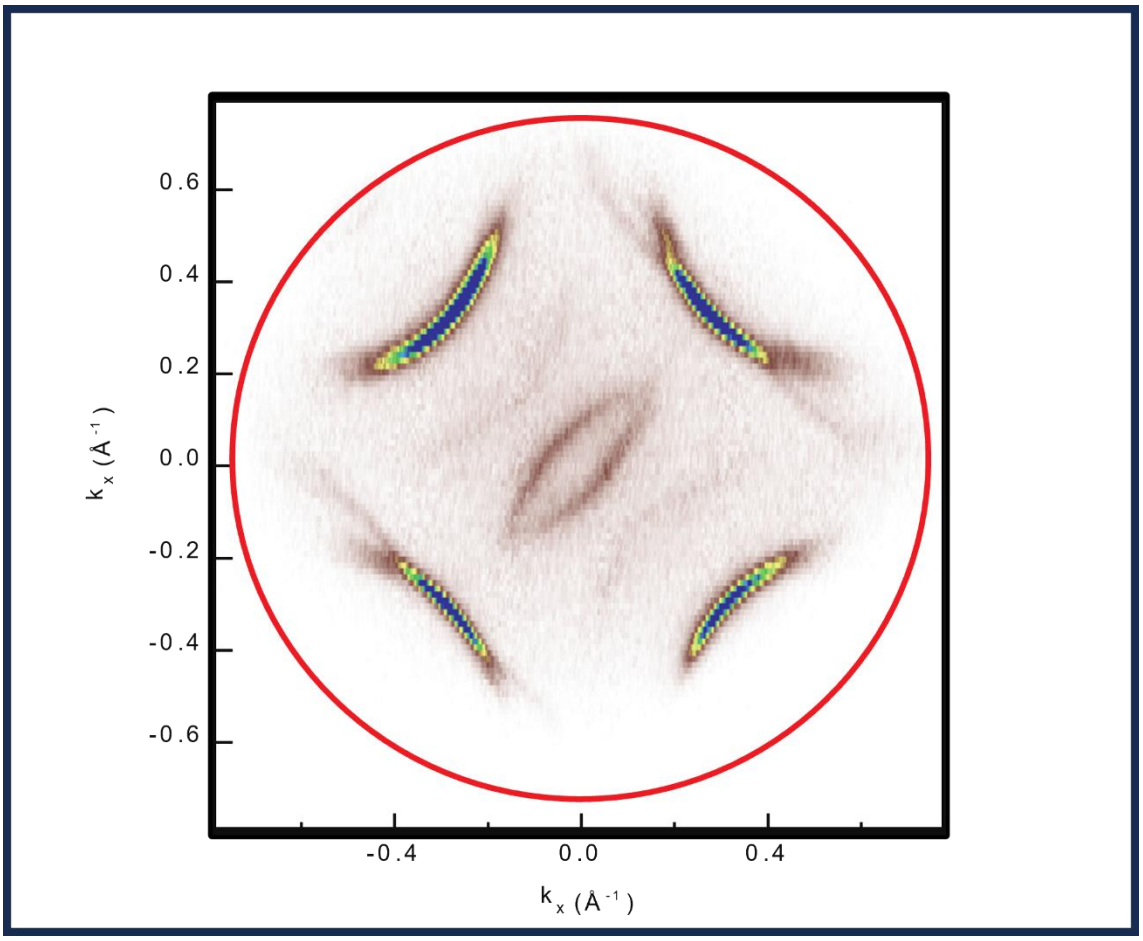

Figure 5. 6: Fermi Surface of Bi2212 with Four Distinct Arcs Captured in a Single ARPES Experiment. The red circle highlights the momentum reach with a diameter of 0.72 Å^{-1}, encompassing almost the full Fermi surface.

Chapter 6: Conclusion

In this work, we have demonstrated the effectiveness of our experimental strategy for acquiring and post processing the full 3D dataset acquired in ARPES measurements under applied bias voltage, building upon the framework introduced by Gauthier et al. (2021). One of the key findings of this study is the consistent nature of the photoemission spectrum across different bias voltages, while simultaneously providing an expanded momentum view, which is crucial for the study of more complex electronic structures.

A particularly significant contribution of our model is the introduction of the ratio limit, which incorporates both the position and angle of electron emission for improved imaging accuracy. This approach can be applied to any system beyond the ASTRAIOS setup, allowing for broader applications. The expanded momentum coverage enabled by our model is especially beneficial for time resolved ARPES experiments, where capturing the full momentum range is essential for analyzing transient states and ultrafast processes.

We showcased our experimental strategy on different samples, namely Au(111), WTe_2, Sr_2RuO_4, and Bi2212. An in-depth analysis of Au(111) showed that while the applied bias voltage expanded the accessible momentum space, the effect on energy resolution was minimal. We observed a minor energy broadening across various bias voltages, with the energy resolution remaining nearly constant.

We also carefully examined the impact of bias on momentum resolution by analyzing the angular spread via momentum distribution cuts (MDCs) taken at 0.48 eV below the Fermi level. The MDCs revealed that as the bias voltage increased, FWHM also increased, indicating a broadening of the angular distribution. This suggests that higher bias voltages lead to a wider spread of photoemitted electrons, primarily due to the electric field focusing electrons emitted at larger angles into the analyzer. Although this broadening enhances the collection of photoemitted electrons, it simultaneously reduces momentum resolution. However, the reduction in momentum resolution was not drastic.

Slit width dependence studies indicated that a narrower slit improved angular resolution, resulting in sharper momentum features. Additionally, these results align with previous studies on Au(111) Rashba splitting and the differences in peak positions observed between kx and ky are likely due to experimental factors such as alignment or detector calibration.

The study of WTe_2 highlighted the anisotropic nature of its electronic structure. With the applied bias voltage and deflector technology, we were able to collect photoemission data and map the momentum space more effectively, despite the challenges posed by the material's complex dispersion. The results

confirmed that the features of the photoemission spectrum remained consistent across the different bias voltages, while also offering an expanded momentum view.

For Sr_2RuO_4, while we successfully collected photoelectrons using lower photon energies and bias voltages, the Fermi surface measurements showed significant distortions, suggesting that such techniques might not be ideal for materials like Sr_2RuO_4. This emphasizes the need for higher photon energies or alternative approaches to minimize distortions.

The ability to map the Fermi surface of Bi2212 using this experimental strategy, capturing all four arcs in a single experiment, marked a significant advancement. This was possible due to the expanded momentum range provided by our biasing technique and deflector technology. The Fermi surface exhibited minimal distortions compared to previous measurements of similar materials, showcasing the potential of this method for high-resolution ARPES experiments on complex superconductors like Bi2212. The ability to capture the entire Fermi surface without the need for sample rotation or multiple measurements offers significant advantages in terms of both time efficiency and experimental consistency.

Overall, our experimental strategy has proven to be an effective and reliable tool for converting 3D ARPES data under bias, enabling the exploration of materials with complex electronic structures. This work sets the stage for future studies where broad momentum views are necessary, without sacrificing the precision or consistency of the core photoemission features.

References

[1] A. Damascelli, “Probing the electronic structure of complex systems by ARPES,” *Phys Scr*, vol. 2004, no. T109, p. 61, 2004.

[2] J. A. Sobota, Y. He, and Z.-X. Shen, “Angle-resolved photoemission studies of quantum materials,” *Rev Mod Phys*, vol. 93, no. 2, p. 025006, 2021.

[3] F. Boschini, M. Zonno, and A. Damascelli, “Time-resolved ARPES studies of quantum materials,” *Rev Mod Phys*, vol. 96, no. 1, p. 015003, 2024.

[4] A. Damascelli, Z. Hussain, and Z.-X. Shen, “Angle-resolved photoemission studies of the cuprate superconductors,” *Rev Mod Phys*, vol. 75, no. 2, p. 473, 2003.

[5] S. V Borisenko, “‘One-cubed’ ARPES user facility at BESSY II,” *Synchrotron Radiat News*, vol. 25, no. 5, pp. 6–11, 2012.

[6] V. N. Strocov *et al.*, “Soft-X-ray ARPES facility at the ADRESS beamline of the SLS: concepts, technical realisation and scientific applications,” *J Synchrotron Radiat*, vol. 21, no. 1, pp. 32–44, 2014.

[7] M. Hoesch *et al.*, “A facility for the analysis of the electronic structures of solids and their surfaces by synchrotron radiation photoelectron spectroscopy,” *Review of Scientific Instruments*, vol. 88, no. 1, 2017.

[8] T. Kiss *et al.*, “A versatile system for ultrahigh resolution, low temperature, and polarization dependent Laser-angle-resolved photoemission spectroscopy,” *Review of Scientific Instruments*, vol. 79, no. 2, 2008.

[9] J. D. Koralek *et al.*, “Experimental setup for low-energy laser-based angle resolved photoemission spectroscopy,” *Review of Scientific Instruments*, vol. 78, no. 5, 2007.

[10] N. Gauthier *et al.*, “Expanding the momentum field of view in angle-resolved photoemission systems with hemispherical analyzers,” *Review of Scientific Instruments*, vol. 92, no. 12, 2021.

[11] H. Hertz, “Ueber einen Einfluss des ultravioletten Lichtes auf die electrische Entladung,” *Ann Phys*, vol. 267, no. 8, pp. 983–1000, 1887.

[12] A. Einstein, “Einstein, a., 1905, ann. phys.(leipzig) 31, 132,” *Ann. Phys.(Leipzig)*, vol. 31, p. 132, 1905.

[13] S. Hüfner, *Photoelectron spectroscopy: principles and applications*. Springer Science & Business Media, 2013.

[14] R. Noguchi, *Designing Topological Phase of Bismuth Halides and Controlling Rashba Effect in Films Studied by ARPES*. Springer Nature, 2022.

[15] M. P. Seah and W. A. Dench, "Quantitative electron spectroscopy of surfaces: A standard data base for electron inelastic mean free paths in solids," *Surface and interface analysis*, vol. 1, no. 1, pp. 2–11, 1979.

[16] Y. Saitoh *et al.*, "Performance of a very high resolution soft x-ray beamline BL25SU with a twin-helical undulator at SPring-8," *Review of Scientific Instruments*, vol. 71, no. 9, pp. 3254–3259, 2000.

[17] S. Souma, T. Sato, T. Takahashi, and P. Baltzer, "High-intensity xenon plasma discharge lamp for bulk-sensitive high-resolution photoemission spectroscopy," *Review of Scientific Instruments*, vol. 78, no. 12, 2007.

[18] G. Liu *et al.*, "Development of a vacuum ultraviolet laser-based angle-resolved photoemission system with a superhigh energy resolution better than 1meV," *Review of Scientific Instruments*, vol. 79, no. 2, 2008.

[19] A. K. Mills *et al.*, "Cavity-enhanced high harmonic generation for extreme ultraviolet time-and angle-resolved photoemission spectroscopy," *Review of Scientific Instruments*, vol. 90, no. 8, 2019.

[20] M. Na, A. K. Mills, and D. J. Jones, "Advancing time-and angle-resolved photoemission spectroscopy: The role of ultrafast laser development," *Phys Rep*, vol. 1036, pp. 1–47, 2023.

[21] X. Zhou, S. He, G. Liu, L. Zhao, L. Yu, and W. Zhang, "New developments in laser-based photoemission spectroscopy and its scientific applications: a key issues review," *Reports on Progress in Physics*, vol. 81, no. 6, p. 062101, 2018.

[22] "ASTRAIOS Preliminary Manual."

[23] E. Benis and T. Zouros, "The hemispherical deflector analyser revisited: II. Electron-optical properties," *J Electron Spectros Relat Phenomena*, vol. 163, pp. 28–39, Apr. 2008, doi: 10.1016/j.elspec.2008.02.001.

[24] H. Zhang *et al.*, "Angle-resolved photoemission spectroscopy," *Nature Reviews Methods Primers*, vol. 2, no. 1, p. 54, 2022.

[25] J. Maklar *et al.*, "A quantitative comparison of time-of-flight momentum microscopes and hemispherical analyzers for time-and angle-resolved photoemission spectroscopy experiments," *Review of Scientific Instruments*, vol. 91, no. 12, 2020.

[26] S. Guo *et al.*, "An ultra-high vacuum system for fabricating clean two-dimensional material devices," *Review of Scientific Instruments*, vol. 94, no. 1, p. 013903, Jan. 2023, doi: 10.1063/5.0110875.

[27] F. Matsui *et al.*, "Bulk and surface band dispersion mapping of the Au (111) surface by acceptance-cone tunable PES system," *e-Journal of Surface Science and Nanotechnology*, vol. 18, pp. 18–23, 2020.

[28] H. Yamane *et al.*, "Acceptance-cone-tunable electron spectrometer for highly-efficient constant energy mapping," *Review of Scientific Instruments*, vol. 90, no. 9, 2019.

[29] Y. Ishida and S. Shin, "Functions to map photoelectron distributions in a variety of setups in angle-resolved photoemission spectroscopy," *Review of Scientific Instruments*, vol. 89, no. 4, 2018.

[30] A. Longa *et al.*, "Time-resolved ARPES with probe energy of 6.0 eV and tunable MIR pump at 250 kHz," *Opt Express*, vol. 32, no. 17, pp. 29549–29557, 2024, doi: 10.1364/OE.525265.

[31] S. LaShell, Ba. McDougall, and E. Jensen, "Spin splitting of an Au (111) surface state band observed with angle resolved photoelectron spectroscopy," *Phys Rev Lett*, vol. 77, no. 16, p. 3419, 1996.

[32] D. P. Woodruff, *Modern techniques of surface science*. Cambridge university press, 2016.

[33] M. Hoesch *et al.*, "Spin structure of the Shockley surface state on Au (111)," *Physical Review B—Condensed Matter and Materials Physics*, vol. 69, no. 24, p. 241401, 2004.

[34] P. Li *et al.*, "Evidence for topological type-II Weyl semimetal WTe2," *Nat Commun*, vol. 8, no. 1, p. 2150, 2017.

[35] Y. Maximenko *et al.*, "Nanoscale studies of electric field effects on monolayer 1T'-WTe2," *NPJ Quantum Mater*, vol. 7, p. 29, Mar. 2022, doi: 10.1038/s41535-022-00433-x.

[36] J. Mesot *et al.*, "Determination of the Fermi surface in high-T c superconductors by angle-resolved photoemission spectroscopy," *Phys Rev B*, vol. 63, no. 22, p. 224516, 2001.

[37] I. M. Vishik *et al.*, "ARPES studies of cuprate Fermiology: superconductivity, pseudogap and quasiparticle dynamics," *New J Phys*, vol. 12, no. 10, p. 105008, 2010.

[38] J. Meng *et al.*, “Coexistence of Fermi arcs and Fermi pockets in a high-T c copper oxide superconductor,” *Nature*, vol. 462, no. 7271, pp. 335–338, 2009.

[39] T. Yokoya, T. Takahashi, T. Mochiku, and K. Kadowaki, “Anomalous band folding due to the BiO superstructure in Bi 2 Sr 2 CaCu 2 O 8 studied by angle-resolved photoemission,” *Phys Rev B*, vol. 50, no. 14, p. 10225, 1994.

[40] V. B. Zabolotnyy *et al.*, “Renormalized band structure of Sr2RuO4: A quasiparticle tight-binding approach,” *J Electron Spectros Relat Phenomena*, vol. 191, pp. 48–53, 2013.

[41] W. Huang, “A review of some new perspectives on the theory of superconducting Sr2RuO4,” *Chinese Physics B*, vol. 30, no. 10, p. 107403, 2021.

[42] K. Fujioka *et al.*, “Electronic structure of SrRuO 3,” *Phys Rev B*, vol. 56, no. 11, p. 6380, 1997.

[43] T. Yokoya *et al.*, “Angle-resolved photoemission study of Sr 2 RuO 4,” *Phys Rev B*, vol. 54, no. 18, p. 13311, 1996.

[44] H. Mizushima *et al.*, “Effect of physisorption of inert organic molecules on Au (111) surface electronic states,” *Physical Chemistry Chemical Physics*, vol. 19, no. 28, pp. 18646–18651, 2017.

[45] F. Reinert, “Spin–orbit interaction in the photoemission spectra of noble metal surface states,” *Journal of Physics: Condensed Matter*, vol. 15, no. 5, p. S693, 2003.

[46] C. Tusche, A. Krasyuk, and J. Kirschner, “Spin resolved bandstructure imaging with a high resolution momentum microscope,” *Ultramicroscopy*, vol. 159, pp. 520–529, 2015.

[47] L. Yang *et al.*, “Highly Tunable Near-Room Temperature Ferromagnetism in Cr-Doped Layered Td-WTe2,” *Adv Funct Mater*, vol. 31, no. 13, p. 2008116, 2021.